



The 2020 Eclipse of R Aquarii in the Near-infrared: Mid-eclipse Observations of Disk Distress

Kenneth H. Hinkle¹ , Sean Brittain² , Francis C. Fekel³ , Thomas Lebzelter⁴ , and Adwin Boogert^{5,6} ¹NSF's National Optical-Infrared Astronomy Research Laboratory, P.O. Box 26732, Tucson, AZ 85726, USA; ken.hinkle@noirlab.edu²Department of Physics and Astronomy, 118 Kinard Laboratory, Clemson University, Clemson, SC 29634, USA³Center of Excellence in Information Systems, Tennessee State University, 3500 John A. Merritt Boulevard, Box 9501, Nashville, TN 37209, USA⁴Department of Astrophysics, University of Vienna, Türkenschanzstrasse 17, A-1180 Vienna, Austria⁵Institute for Astronomy, University of Hawaii at Manoa, 2680 Woodlawn Drive, Honolulu, HI 96822, USA

Received 2022 March 17; revised 2022 July 25; accepted 2022 August 15; published 2022 October 3

Abstract

The Mira in the bright, dusty, symbiotic binary R Aquarii undergoes eclipses of multiyear duration every ~ 44 yr by a large, opaque accretion disk. The 2020 eclipse was confirmed by *I*-band photometry. High-resolution *M*- and *K*-band spectra were observed near the midpoint of the eclipse, in 2020 August and September. The $4.5\text{--}5.5\ \mu\text{m}$ spectrum during eclipse is a complex blend of disk and Mira features. Continuum emission from the disk region contributes to both the $2.3\ \mu\text{m}$ and $4.6\ \mu\text{m}$ region. The lowest energy vibration-rotation CO lines contain multiple absorption features from ~ 780 K gas flowing across the disk away from the Mira. CO fundamental and overtone emission lines are also present. The eccentricity of the orbit results in significant orbital variation in the size of the Roche lobes. At periastron the Roche radius of the secondary is ~ 4.0 au, smaller than both the 5 au geometric radius for the disk and estimates for the disk size from models. Fundamental band CO 2–1 emission originates from a thin, eccentric ring with inner radius ~ 4.75 au and outer radius ~ 6.9 au. The CO emission is identified with regions where the disk has been disrupted near the time of periastron. CO 3–2 fundamental band lines and low-excitation lines in the CO 2–0 and 3–1 overtone bands originate in a Mira-facing spot, 6.3 au from the accretion disk center, near the inner Lagrange point.

Unified Astronomy Thesaurus concepts: [Eclipsing binary stars \(444\)](#); [Circumstellar matter \(241\)](#); [Mira variable stars \(1066\)](#); [Multiple star evolution \(2153\)](#); [Stellar accretion disks \(1579\)](#); [Symbiotic binary stars \(1674\)](#)

1. Introduction

The Mira variable R Aquarii (R Aqr) is among the visually brightest variable stars, designated HR 8992 in the Yale Bright Star Catalog (Hoffleit & Jaschek 1982). Known as a variable star since 1811, spectra taken at Mt. Wilson in 1922 revealed a hot companion to the Mira (Merrill 1935). The companion was subsequently shown to be a white dwarf (WD) with temperature $\sim 60,000$ K and luminosity $\sim 1 L_{\odot}$ (Burgarella et al. 1992; Meier & Kafatos 1995; Contini & Formigini 2003). Merrill (1950) and, later, Allen (1984) listed the R Aqr system as a “symbiotic” (SySt), one of the several classes of widely separated, mass-transfer binary systems consisting of an evolved star and a hot, degenerate object (Escorza et al. 2020). SySt typically are detached with a M-giant primary and a WD companion. R Aqr is among the nearest of the SySt.

R Aqr has a large infrared (IR) excess, and thus falls into the dusty or D-type symbiotic subclass, SySt-D. In such systems the primary is a pulsating asymptotic giant branch (AGB) star with large mass loss, typically, as in R Aqr, a Mira. In fact, the closest SySt-D, but with a wider separation between the Mira and WD than R Aqr, is the prototype Mira omicron Ceti (*o* Ceti; Karovska 2006).

Based on a compilation of visual photometry for R Aqr by Mattei & Allen (1979) that spans more than a century from

1846 to 1979, Willson et al. (1981) found that the Mira is eclipsed at an interval of ~ 44 yr by an unseen, opaque body. Due to the Mira’s long period, large visual amplitude, and variable maxima and minima magnitudes, the eclipses went undetected for a century. Willson et al. (1981) found the eclipses to last $\lesssim 8.5$ yr, placing the middle of the next eclipse before or in 2023. Microwave images of the mass flow between the R Aqr Mira and WD confirm that interbinary material will eclipse the Mira starting in ~ 2020 (Bujarrabal et al. 2018). Teyssier et al. (2019) report that the eclipse started in 2019.

The type of eclipse reported for R Aqr is a “disk eclipse” (Hajduk et al. 2008). Known objects of this type are rare⁷ due to long orbital periods and difficulties discerning eclipses from stellar variability. As is the case for R Aqr, imaging techniques have confirmed that the eclipsing body in these systems is a dusty disk around a companion star or degenerate secondary, with mass loss from a giant/supergiant being accreted onto the disk (see, for instance, Kloppenborg et al. 2015). The known group of disk-eclipse systems is small; partial lists can be found in Hajduk et al. (2008) and Rattenbury et al. (2015). The post-AGB supergiant Epsilon Aurigae (ϵ Aur) is the prototype system. The F-type supergiant post-AGB star in the ϵ Aur system (Parthasarathy & Muneer 2019) evolved from a massive AGB star and has a B-type companion embedded in an optically thick accretion disk (Kloppenborg et al. 2010; Strassmeier et al. 2014). ϵ Aur has an orbital period of

⁶ Visiting Astronomer at the Infrared Telescope Facility

⁷ Many eclipsing SySt systems are known but these are mainly “S-type” (SySt-S), where the primary star eclipses the secondary. S-type symbiotics are characterized by lack of a strong IR excess. The IR spectral energy distribution is that of a cool star (Webster & Allen 1975). In typical SySt-S a hot degenerate accretes mass from an early-M giant that is a low-amplitude variable.

Table 1
Summary of Observations

HJD	Date	Pulsation Phase	Observatory/ Spectrograph	Resolution ($R = \lambda/\Delta\lambda$)	Wavelength Range (μm)	Integration Time (min.)	S/N (Peak)
2447540.490	1989 Jan 13	0.23	KPNO/4 m FTS	70000	1.5–2.5	35	164
2447546.513	1989 Jan 19	0.25	KPNO/4 m FTS	126000	4.54–4.76	130	102
2459070.168	2020 Aug 8	0.08	NASA IRTF/iSHELL	88100	4.56–5.10	5	>200
2459112.964	2020 Sep 20	0.19	NASA IRTF/iSHELL	88100	4.56–5.10	5	>200
2459113.025	2020 Sep 20	0.19	NASA IRTF/iSHELL	88100	2.18–2.47	2	>100

27.1 yr with an eclipse duration of 1.5 yr. In addition to R Aqr, another bright, late-type, disk-eclipse system is V Hydrae (V Hya). In the case of V Hya, the Mira primary is carbon-rich in a 17 yr orbit with an unseen companion (Knapp et al. 1999).

Given the importance of mass loss and accretion processes to astrophysics, the disk eclipse of the R Aqr Mira presents a valuable opportunity to study a nearby accretion disk and to place observational constraints on mass exchange and accretion processes. Photometry of previous eclipses demonstrates that the R Aqr eclipse is not total; the Mira pulsation is visible throughout the eclipse. Previous eclipse observations appearing in the literature were taken by chance. This eclipse is the first opportunity to plan observations of the eclipse.

This paper reports on the 2–5 μm IR spectrum of R Aqr observed at high resolution during the eclipse. Section 2 describes the observations and reductions, both for our spectra and for the literature photometry used in phasing the eclipse. Section 3 reviews the features of the spectra. Section 4 contains a brief literature review that highlights features of R Aqr pertinent to the current paper. Interpretation of the current observations follows in Section 5. Section 6 summarizes the new insights into the R Aqr system resulting from this work.

2. Observations and Reductions

2.1. Infrared Spectroscopy

R Aqr was observed on 2020 August 8 in the M band and on 2020 September 20 in the M and K bands with the immersion grating echelle spectrograph (iSHELL) on the National Aeronautics and Space Administration Infrared Telescope Facility (NASA IRTF) 3.2 m telescope (Table 1). The spectrum of the M band is dominated by the vibration-rotation CO fundamental. The long-wavelength region of the K band is dominated by the vibration-rotation CO first overtone. iSHELL is a cross-dispersed, high-resolution spectrometer with wide wavelength coverage (Rayner et al. 2022). The M -band iSHELL observations used the “M1” mode. In the M1 mode most of the M -band window, 4.56–5.10 μm (1960–2191 cm^{-1}), is covered by a single iSHELL observation. Small gaps do exist between orders. The K -band iSHELL observation used the “Kgas” mode. Kgas covers 2.18–2.47 μm (4049–4587 cm^{-1}). The spectral resolution, $R = \lambda/\Delta\lambda$, for all three observations is $88,100 \pm 2000$, i.e., $\sim 3.4 \text{ km s}^{-1}$. The spectrograph slit width was $0''.375$. The details of the observations appear in Table 1. The spectra were reduced using standard iSHELL reduction techniques. Systematic effects, including the blaze shape, were removed with a reference flat.

A synthetic telluric spectrum was used to remove the telluric spectrum from the M - and K -band spectra. While many lines can be successfully removed by ratioing the observed spectrum to a telluric spectrum, for the strongest telluric lines no stellar

information can be recovered. This is a major observational difficulty in the M band, where the low-excitation, telluric CO lines are optically thick and can obscure key astronomical lines. Since the signal-to-noise ratio (S/N) in the ratioed spectrum is dependent on the optical depth of the telluric features that have been removed, the ratioed spectrum does not have uniform S/N. The R Aqr iSHELL observations were scheduled at a favorable heliocentric Doppler shift due to the orbital motion of the Earth so the low-excitation R Aqr CO lines are observable. The August shift is larger than that in September.

R Aqr is very bright throughout the mid- and near-IR, $M \approx -2.5$ and $K \approx -1.6$, out of eclipse. As one of the brightest Miras, it was observed with the Fourier Transform Spectrometer (FTS) at the Kitt Peak National Observatory (KPNO) 4 m telescope (Hall et al. 1979) in the 1980s and early 1990s (Hinkle et al. 1989). The FTS archives (Pilachowski et al. 2017) contain one high-resolution M -band spectrum, observed on 1989 January 19 (Table 1). Unfortunately, the heliocentric velocity shift on this date is not sufficient to separate the low-excitation R Aqr and telluric CO lines. Nonetheless, this observation provides a valuable out-of-eclipse reference spectrum. The resolution of the M -band FTS spectrum, 2.4 km s^{-1} , is ~ 1.4 times higher than that of the iSHELL spectrum.

The FTS archives contain a number of high-resolution K -band FTS spectra (Table 1 of Hinkle et al. 1989). The resolution for FTS spectra is fixed in wavenumber across the entire spectral range. For the R Aqr K -band spectra this is typically 0.07 cm^{-1} , i.e., 4.9 km s^{-1} in the $2.3 \mu\text{m}$ CO $\Delta v = 2$ region. The K -band resolution of the iSHELL spectra is ~ 1.5 times higher than that of the FTS spectra. The Mira photospheric features are resolved at the FTS resolution (Hinkle et al. 1989).

The pulsation period of R Aqr was shown to be stable for more than 100 yr at 387–390 days by Campbell (1955) and Mattei & Allen (1979). This period has been confirmed from recent observations by Hartig et al. (2022). However, times of individual maxima can vary by 20 days or more, i.e., 0.05 in phase (Kurochkin 1976; Gromadzki & Mikołajewska 2009). The tentative light-curve phases of the 2020 August and September observations are 0.08 and 0.19, respectively. Phase 0.0 is defined as the visual light maximum. The M -band FTS spectrum was observed at phase ~ 0.25 . Phases have been calculated by fitting the visual light curves.

From the orbit of Gromadzki & Mikołajewska (2009) the center-of-mass velocity⁸ of the Mira in 2020 August–September was $\sim -24 \text{ km s}^{-1}$. The center-of-mass velocity for the Mira in 1989 was -29 km s^{-1} (Hinkle et al. 1989; Gromadzki & Mikołajewska 2009). Adopting the mass ratio

⁸ The velocities used in this paper are heliocentric. To convert to LSR subtract 1.18 km s^{-1} .

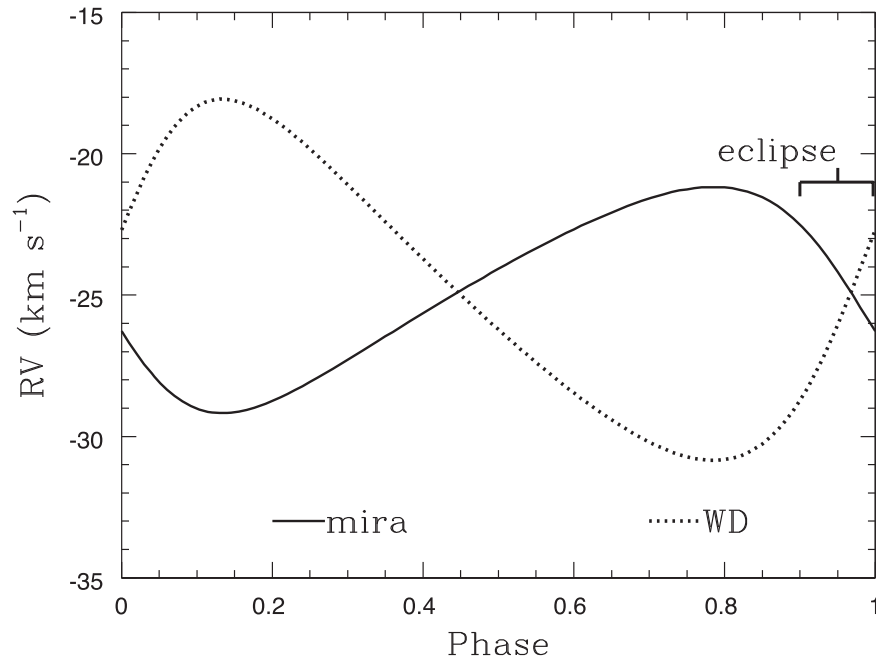


Figure 1. Radial velocity as a function of orbital phase for the R Aqr Mira and WD from the orbital elements of Gromadzki & Mikołajewska (2009). The WD orbit, which is not observed, assumes the ratio of the Mira to WD mass is 1.6. Zero phase is a time of periastron passage. A disk eclipse of duration one-tenth the orbital period, 4.4 yr, is marked. The characteristics of the eclipse are not well known. Ingress and egress times could differ significantly from those shown.

estimated by Gromadzki & Mikołajewska (2009), $M_{\text{Mira}}/M_{\text{WD}} = 1.2\text{--}2.1$, the velocity of the WD can be computed (Figure 1). In 2020 August–September, the WD velocity was ~ -27 to -25 km s^{-1} .

2.2. Photometry

Whitelock et al. (1983) demonstrated that near-IR wavelengths, where the diameter of the Mira reaches its minimum and there is no contribution from IR excess, are optimum for monitoring the onset and duration of the eclipse of the R Aqr Mira by the secondary disk. Whitelock et al. (1983) utilized *JHKL* photometry but noted the special usefulness of the *J* band. Jurkic & Kotnik-Karuzza (2018) produced an eclipse curve from the *J*-band data of Whitelock et al. (1983) and Catchpole et al. (1979). The eclipse is clearly shown in Figure 1 of Jurkic & Kotnik-Karuzza (2018), where the pulsation light curve of the Mira has been ratioed from the observations. Unfortunately the sampling during the late 1970s eclipse was fairly sparse. Photometry presented by Jurkic & Kotnik-Karuzza (2018) places mid-eclipse at about JD 2443000, 1976 August. Taking the orbital period of 43.6 yr, the middle of the current eclipse is predicted for \sim JD 2458900, 2020 March, eight months before the conjunction mid-date of 2020 November calculated from the orbit (Section 4.1).

Since the 1970s and 1980s the sensitivity of IR detectors has greatly improved. Stars with *J* magnitudes as bright as R Aqr saturate newer devices on research-size telescopes. While it is possible that the current eclipse has been monitored in the near-IR, we know of no data. However, charge-coupled device (CCD) detectors are now available to amateur astronomers and can be mounted on telescopes appropriately sized to observe bright stars. There is an increasing number of *I*-band observations reported from these devices. In Figure 2 observations of R Aqr in the *I* band, made available through the American Association of Variable Star Observers (AAVSO), are plotted. A typical *I*-band light curve for the R

Aqr Mira was extracted from the data and then divided into the light curve. The resulting eclipse curve is shown in Figure 2. Assuming a 15,943 day orbital period (Gromadzki & Mikołajewska 2009) and a nominal *J*–*I* value of 2.97 for R Aqr, the *J*-band eclipse curve of Jurkic & Kotnik-Karuzza (2018) was connected to these data. A more refined reduction employing a time series of post-eclipse *I*-band data could provide additional insight into the eclipse. In any case, it is clear that mid-eclipse did occur near 2020 March. The near-IR spectra were taken slightly past mid-eclipse. Given the multiyear eclipse duration, the data are representative of the mid-eclipse period.

3. Analysis of the Spectra

3.1. *M*-band Overview

Figure 3 shows a segment, $2138\text{--}2148$ cm^{-1} ($4.655\text{--}4.677$ μm), of the R Aqr spectrum observed both out of eclipse in 1989 and during the disk eclipse in 2020⁹. The region shown spans a few percent of the iSHELL observation, from the CO 1–0 P(1) to the 1–0 R(0) line, arguably the least-blended 4.6 μm region. Nonetheless, the out-of-eclipse spectrum contains a rich array of photospheric CO lines from the Mira. Lines from CO isotopologues as well as from H₂O are also found in this interval. Spectra from both iSHELL observations, 2020 August and September, are shown over-plotted. There is little change in the *M*-band spectrum during the 43 days between the observations. The complexity of the in-eclipse spectra is striking. In particular, there are no deep lines, including the lowest excitation CO lines.

Also included in Figure 3 is a spectrum of HR 4049 (Hinkle et al. 2007), a post-AGB supergiant with a low-mass companion in a circumbinary disk. In this wavelength region

⁹ Based on the photometric evidence for the eclipse (Section 2.2), the 2020 spectra will be referred to as “in-eclipse” spectra. Archival spectra will be referred to as “out-of-eclipse” spectra.

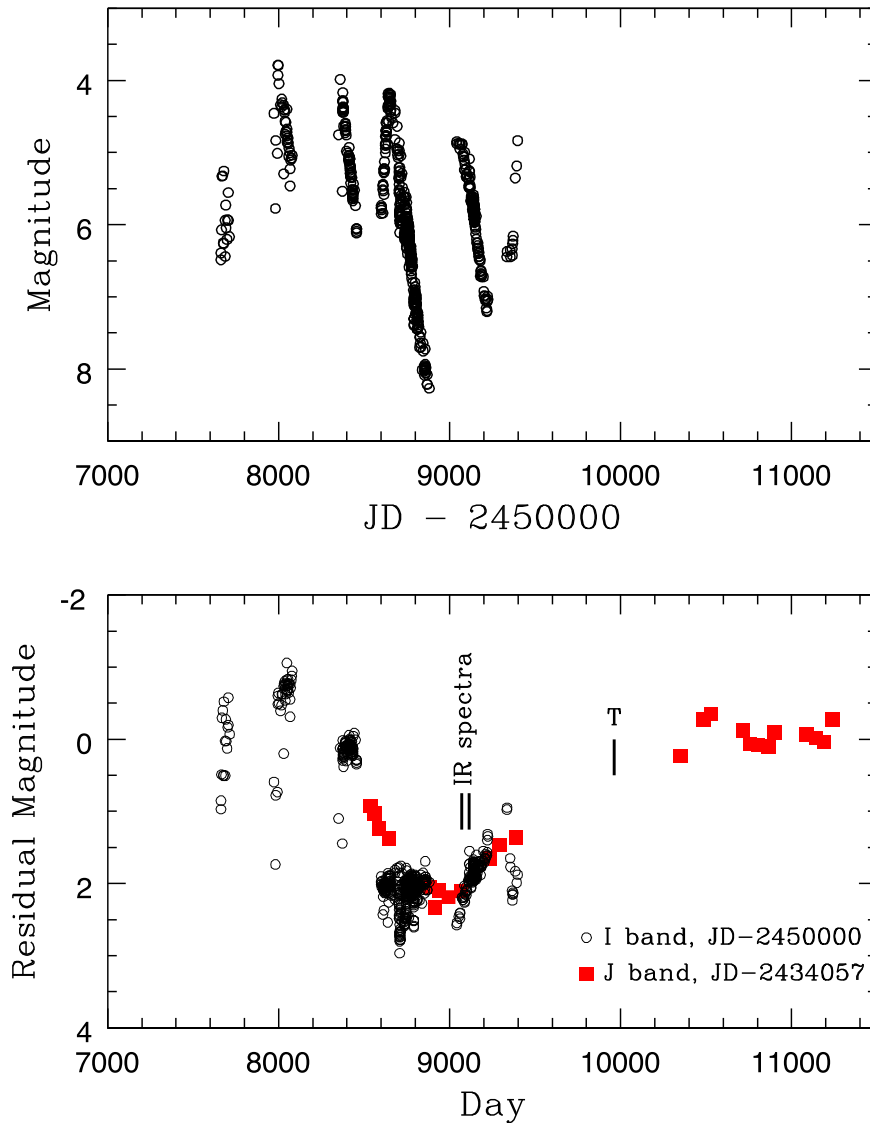


Figure 2. Upper panel: AAVSO *I*-band photometry of R Aqr (black open symbols). Segments from several light cycles are present. Lower panel: data in upper panel ratioed to a mean light curve. The *J*-band eclipse light curve of Jurkic & Kotnik-Karuza (2018, red filled symbols) is shown shifted by one orbital period, corrected for the mean *J-I* color, and overplotted on the *I* photometry. The dates of the IR spectra and the predicted date of periastron passage (T) are shown.

the HR 4049 spectrum consists of emission lines with an excitation temperature of ~ 600 K superimposed on an otherwise featureless dust continuum. Comparison of this spectrum to that of R Aqr confirms the presence of emission lines from both CO and H₂O in the R Aqr spectra.

Archival spectra (Pilachowski et al. 2017) show that the out-of-eclipse $4.6 \mu\text{m}$ spectrum has photospheric lines about $\sim 30\%$ less deep than for a “typical” late-M Mira. Mira spectral line profiles vary with the pulsation phase. Fortunately, the phases of the out-of-eclipse and in-eclipse R Aqr spectra are similar (Table 1). The in-eclipse lines are more shallow than the out-of-eclipse lines. We attribute veiling from disk emission to the shallow out-of-eclipse line depth. Veiling combined with the obscuration of the Mira further reduce the line depth during eclipse. The spectra are not flux calibrated and it is not possible to quantify the changes in the continuum flux. Comparison with other SySt-D spectra, which are not eclipsed, shows varying contributions of dust continuum at $4.6 \mu\text{m}$. Spectra of HM Sagittae have a featureless continuum with low-excitation lines in emission. V1016 Cygni (V1016 Cyg) has heavy dust

veiling with P-Cygni-type profiles for the low-excitation lines. V407 Cyg has a Mira absorption line spectrum but with shallow lines (see Figure 21 of Hinkle et al. 2013).

In the out-of-eclipse R Aqr Infrared Space Observatory (ISO) spectral energy distribution (SED) the Mira photosphere dominates from optical wavelengths through $2.5 \mu\text{m}$ (Mayer et al. 2013). At $4.6 \mu\text{m}$ there is an $\sim 30\%$ IR excess. Omelian et al. (2020) show that the $12.19 \mu\text{m}$ flux is dependent on both orbital phase and pulsation phase, with the pulsation phase dominant and brighter near Mira pulsation maximum. ISO observations were taken at orbital phase 0.389, with orbital phase 0.0 defined at periastron, and pulsation phase 0.14. The out-of-eclipse $4.6 \mu\text{m}$ archival spectrum was observed at similar orbital phase, 0.221, and pulsation phase, 0.25. The results of Omelian et al. (2020) suggest that the contribution of the dust continuum to the eclipsed spectrum could vary significantly with the pulsation phase of the Mira. The IR spectra (Table 1) were all taken near maximum light.

A comparison of the spectra in Figure 3 shows that the in-eclipse R Aqr spectra observed in 2020 consist of a

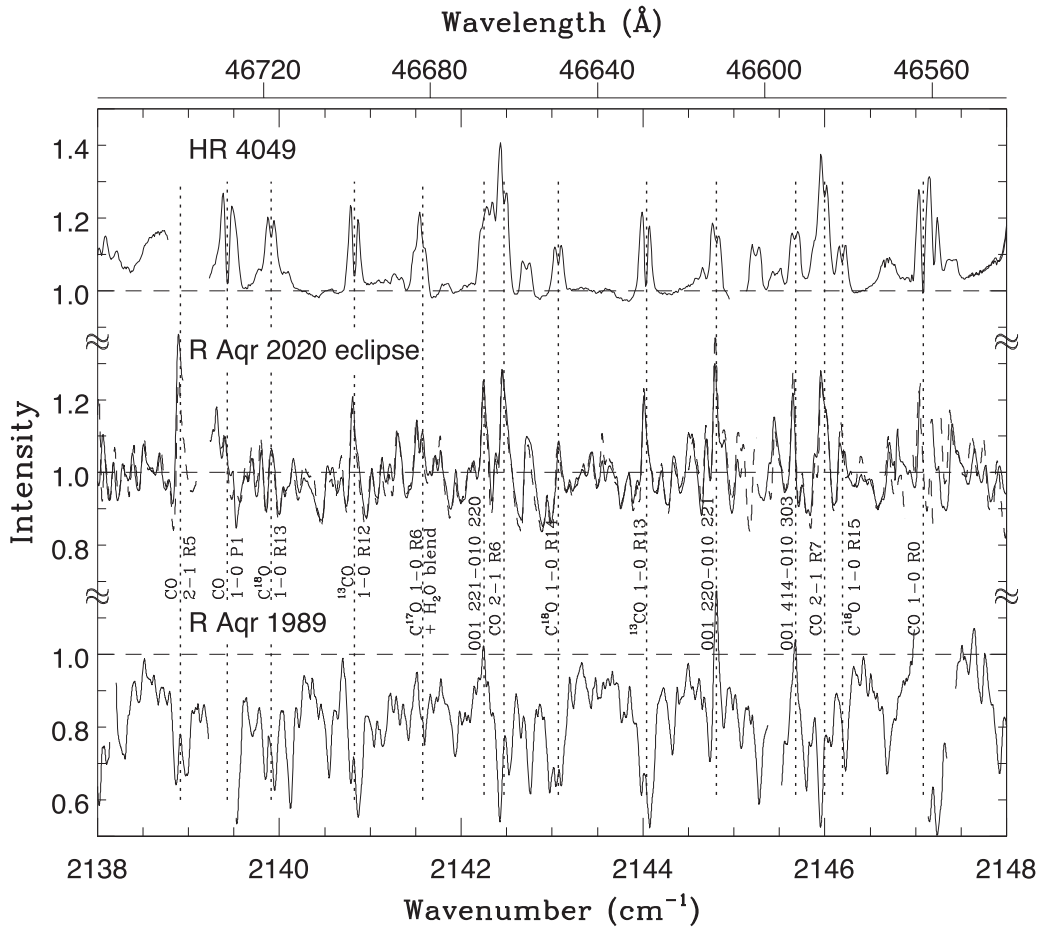


Figure 3. A segment of the observed R Aqr *M*-band spectra in and out of eclipse. The spectrum of HR 4049, which is dominated by a circumbinary disk, is shown as a comparison. A selection of the emission lines are identified. The spectra have been ratioed to a telluric reference to remove the telluric spectrum. The wavenumber/wavelength scale is at laboratory rest with the spectra shifted to align the emission lines. Absorption line spectra of Miras contain multiple velocity components (Figure 4). The Mira absorption lines are at a slightly different velocity than the emission lines due to the multiple velocity components, Mira pulsation, and orbital motion. The gaps in the spectrum result from optically thick telluric lines that cannot be removed by ratioing. The two R Aqr spectra, observed in 2020 August, shown with a solid line, and September, shown with a dashed line, have been overlapped and are nearly identical.

combination of disk emission lines, Mira absorption lines, and continuum emission. The emission lines differ notably from those of HR 4049 in being neither as broad nor conspicuously double peaked. However, the range of emission lines present indicates that the excitation temperature is similar in R Aqr and HR 4049. Emission lines from the ^{13}CO isotopologue are present in R Aqr but the lines of rare isotopologues are, unlike in the HR 4049 spectrum, not conspicuous. Most of the emission lines and some low-excitation absorption lines seen in the 2020 R Aqr spectra are not present in the 1989 R Aqr spectrum and must be features of the eclipse.

A detailed examination of the entire in-eclipse *M*-band spectrum reveals emission lines from the $^{12}\text{C}^{16}\text{O}$ 1–0, 2–1, and 3–2 bands, peaking at rotational transition $J'' \sim 12$. Emission can also be seen in the $^{13}\text{C}^{16}\text{O}$, $^{12}\text{C}^{18}\text{O}$, and H_2O lines. Some of the emission lines appear to have strengthened a few percent from August to September. Shallow, broad, low-excitation CO absorption related to the eclipse is present. We review each of these sets of lines below.

3.2. *M*-band Mira Spectrum

Mira variables have complex spectra. Up to three atmospheric regions contribute to line profiles in Miras, a pulsating photosphere, an infalling, semi-stationary, roughly 1000 K

region, and an expanding circumstellar shell (Hinkle et al. 1982). Near-IR spectra are dominated by photospheric lines undergoing large-amplitude velocity shifts due to the stellar pulsation. In the case of R Aqr, the pulsation amplitude is $\sim 30 \text{ km s}^{-1}$ with a discontinuous velocity curve, i.e., the lines double near maximum light (Hinkle et al. 1989). The 1000 K molecular component, seen in the near-IR in low-excitation CO and H_2O lines, undergoes small-amplitude variations of a few kilometers per second and is typically at an infall (redshifted) velocity of $\sim 10 \text{ km s}^{-1}$ relative to the center-of-mass velocity (Hinkle et al. 1982). SiO masers originate in or near the same atmospheric region (Ragland et al. 2008) as well as absorption lines observed against the radio photosphere (Reid & Menten 1997).

The archival 1989 and iSHELL 2020 spectra were taken at similar light-cycle phases. The 1989 line profiles have two velocity components at ~ -32.5 and -19.1 km s^{-1} . The center-of-mass radial velocity for the Mira in the 1989 spectrum is $\sim -29 \text{ km s}^{-1}$ (Table 4 of Hinkle et al. 1989). For 2020 the Mira is at a post-maximum phase where two photospheric velocity components are present. These are offset -2 and $+15 \text{ km s}^{-1}$ relative to the Mira center-of-mass velocity of -24 km s^{-1} (Gromadzki & Mikołajewska 2009), i.e., at -26 and -9 km s^{-1} . The orbital motion results in a 5 km s^{-1} shift

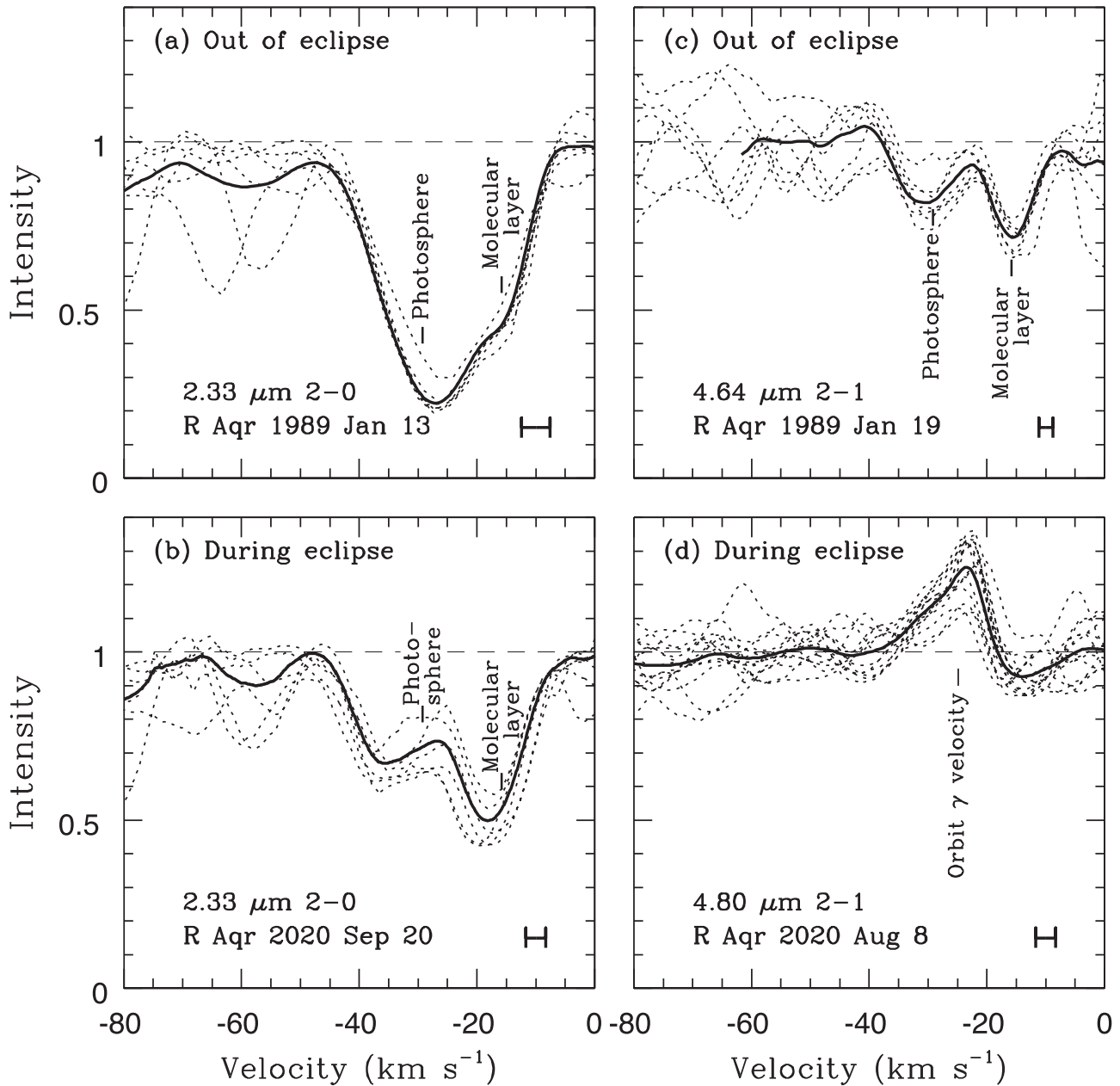


Figure 4. Comparison of R Aqr line profiles in and out of eclipse. Individual line profiles are shown with a dotted line and the average with a solid line. The spectra have been ratioed to a telluric standard. (a) *K*-band CO 2–0 lines from a 1989 out-of-eclipse spectrum and (b) from the 2020 September in-eclipse spectrum. Note the difference in the depth and shape of the line profile out of eclipse and during eclipse. Individual profiles are $^{12}\text{C}^{16}\text{O}$ 2–0 R1, R3, R4, R7, and R10. (c) *M*-band CO 2–1 lines from a 1989 out-of-eclipse spectrum and (d) from the 2020 August in-eclipse spectrum. The 2–1 absorption lines outside of eclipse are in emission during eclipse. Individual profiles are $^{12}\text{C}^{16}\text{O}$ 2–1 R6, R7, R8, R9, R11, R13, and R14. The 2–1 R6 and R7 lines are in the segment of the spectrum shown in Figure 3. To compare scales, 0.1 cm^{-1} (2.5 \AA) is $\sim 15\text{ km s}^{-1}$ in the 2000 cm^{-1} (50000 \AA) region. The 1989 spectra have been corrected by the difference in orbital velocity to the velocity of the 2020 August spectrum. The “photospheric” and “molecular layer” labels mark velocities measured from the 1989 January 13 spectrum and corrected by the orbital velocity to 2020 August. A bar of length equal to the spectral resolution is in the lower right of each panel.

relative to the lines in the 2020 spectra. In addition, the low-excitation lines should have absorption at $\sim +10$ relative to the center-of-mass velocity from the semi-stationary 1000 K region. In the iSHELL 2020 spectra this component is at $\sim -14\text{ km s}^{-1}$. The 1000 K and photospheric lines have a FWHM of $\sim 10\text{ km s}^{-1}$ so the -9 and -14 km s^{-1} components are blended in the iSHELL spectra. These velocity components are seen in both the in-eclipse and out-of-eclipse *K*-band spectra (Section 3.5) as well as in the out-of-eclipse *M*-band spectra (Figure 4).

3.3. In-eclipse *M*-band Emission Lines

3.3.1. CO

Figures 4 and 5 show an overview of the 1–0, 2–1, and 3–2 ^{12}CO line profiles comparing the profiles in and out of eclipse. ^{13}CO 1–0 emission is also present (Figure 3), as is C^{18}O but the latter lines are weak. Line blending in the complex spectrum and the residuals from the removal of the telluric spectrum make individual line profiles noisy. In Figures 4 and 5, lines are grouped by vibrational transition with an average profile

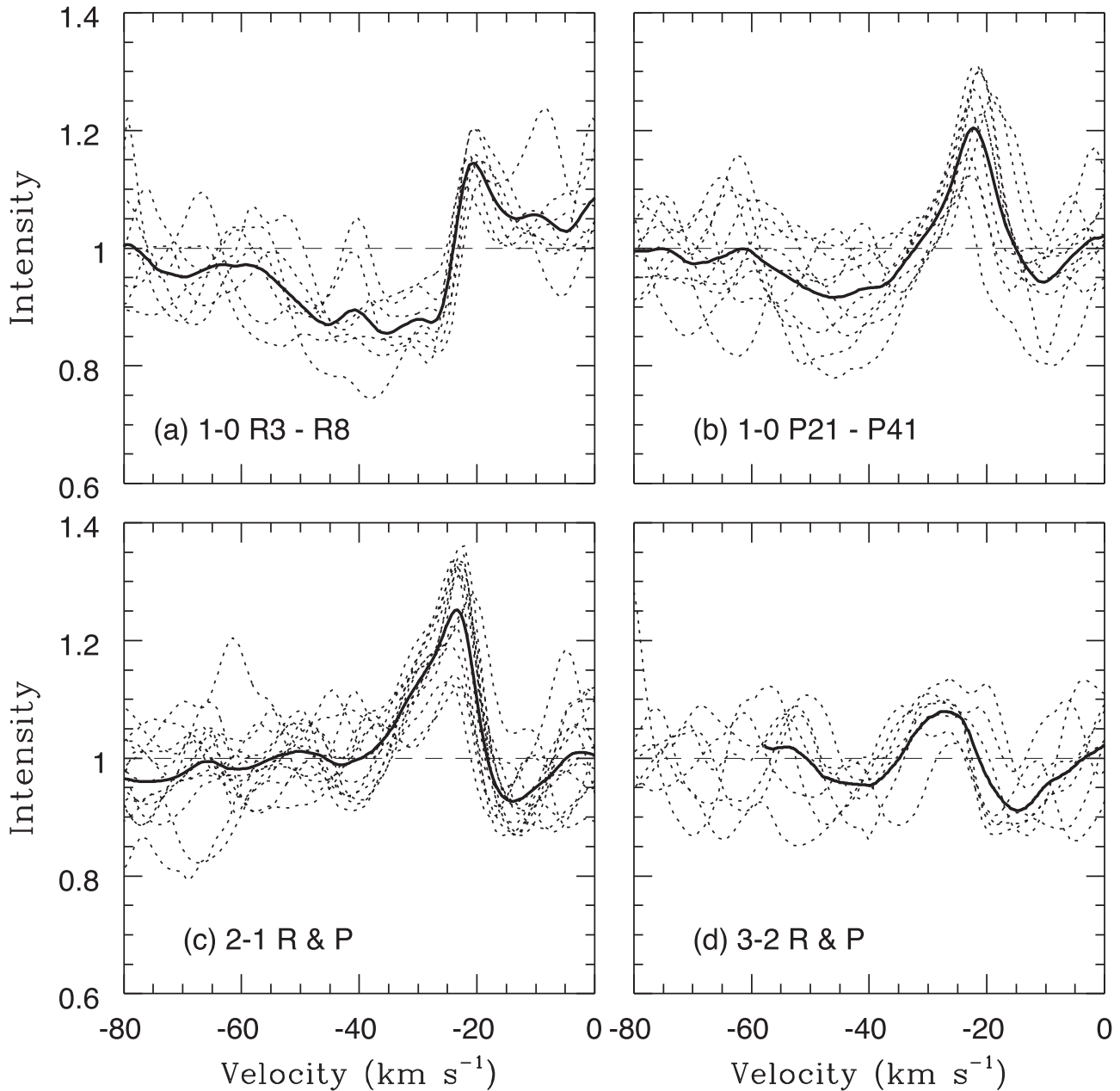


Figure 5. Four different groups of CO lines observed in the 2020 August iSHELL in-eclipse spectrum. Note that the origin of the intensity axis is 0.6. Individual line profiles are shown with a dotted line and the average with a solid line. (a) $^{12}\text{C}^{16}\text{O}$ 1–0 R3 through R8. Emission is near -21 km s^{-1} with absorption extending from ~ -25 to -60 km s^{-1} . (b) 1–0 P $J'' = 21, 22, 26, 27, 30, 32, 34, 35, 38,$ and 41 . Broad blueshifted absorption is present but less deep than for the 1–0 R3 through R8 lines. The emission is stronger than for the lower J'' lines. (c) 2–1 P $J'' = 18, 19, 22, 25, 28, 32,$ and 33 and R $J'' = 7, 8, 9, 11, 13, 14,$ and 20 . There is no absorption in the 2–1 profile in the -60 to -20 km s^{-1} region. The absorption at $\sim -15 \text{ km s}^{-1}$ is from the stellar photosphere and molecular layers (see Figure 4 and text). (d) 3–2 P14, P15, P19, R14, R16, R21, and R23. Emission is weak.

shown. The iSHELL instrumental profile, 3.4 km s^{-1} FWHM, resolves the line profiles but results in smoothing (Figure 4).

As a result of the strong $5 \mu\text{m}$ telluric ozone band, the observable parts of the 1–0 band are broken into two sections, the low-excitation R branch from $J'' 0$ to 10 and the P branch from $J'' \approx 30$ to >50 . Emission can be seen as high as $J'' \approx 41$. The in-eclipse line profiles have broad absorption to the blue and emission to the red. No out-of-eclipse reference line profiles exist for the 1–0 lines due to the strong telluric CO lines and the limited wavelength coverage of the out-of-eclipse spectrum.

The 3–2 emission is weak and detectable only from $J'' \approx 14$ to 23. Hence, the best in-eclipse emission line data are provided

by the 2–1 band. The in-eclipse 2–1 emission peaks at $\sim -23.5 \pm 0.2 \text{ km s}^{-1}$ with a second possible peak at $\sim -30 \text{ km s}^{-1}$ (Figure 5). The CO emission peak velocity has a marked trend with excitation energy (Figure 6). The observed range of velocities is $\sim 8 \text{ km s}^{-1}$ with the lowest excitation emission at -19 km s^{-1} and the highest excitation emission at -26 km s^{-1} .

The peak 2–1 emission intensity is at $J'' \approx 12$ and can be traced to $J'' \approx 35$ (Figure 5). In the optically thin case the J'' of peak emission corresponds to an excitation temperature of $\sim 1000 \text{ K}$. Assuming a single excitation temperature, a curve of growth analysis gives an excitation temperature for the emission of $1200 \pm 200 \text{ K}$. The emission completely fills the

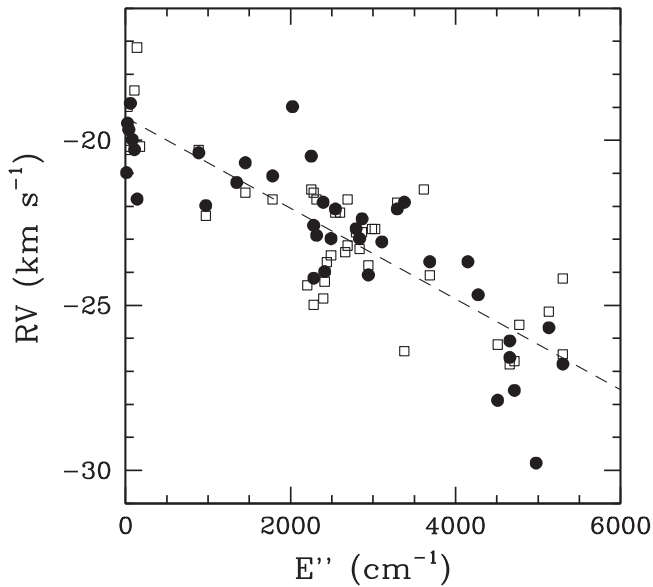


Figure 6. Radial velocity of the peak emission of $^{12}\text{C}^{16}\text{O}$ lines as a function of the lower-level excitation energy of the transition. Filled symbols are from 2020 August, open symbols are from 2020 September. The dashed line is a linear fit to the data. The systemic velocity of the binary is $-24.9 \pm 0.2 \text{ km s}^{-1}$ (Gromadzki & Mikołajewska 2009) with the Mira velocity $\sim -24 \text{ km s}^{-1}$ and the WD velocity $\sim -27 \text{ km s}^{-1}$ on the dates of the observations.

photospheric component seen in the out-of-eclipse lines at -26 km s^{-1} (Figure 4). The emission inflects at this point. The FWHM is 9.5 km s^{-1} . The profile is decidedly asymmetric.

The isotopic abundances allow a novel check on the excitation temperature. Photospheric carbon and oxygen isotopic ratios for the R Aqr Mira are reported in Hinkle et al. (2016) based on a high-resolution $1.5\text{--}2.5 \mu\text{m}$ spectrum observed on 1983 September 14, $^{12}\text{C}/^{13}\text{C} = 16 \pm 5$, $^{16}\text{O}/^{17}\text{O} = 2344 \pm 1000$, and $^{16}\text{O}/^{18}\text{O} = 112 \pm 40$, based on a single line. To confirm the isotopic ratios we repeated the analysis on a high-resolution $1.5\text{--}2.5 \mu\text{m}$ spectrum observed on 1989 January 13 (Pilachowski et al. 2017). In agreement with the earlier result, $^{12}\text{C}/^{13}\text{C} = 11 \pm 5$, $^{16}\text{O}/^{17}\text{O} = 3735_{-1600}^{+2800}$, and $^{16}\text{O}/^{18}\text{O} = 216_{-190}^{+1500}$. Comparing the $^{12}\text{C}^{16}\text{O}$ and $^{13}\text{C}^{16}\text{O}$ emission line strengths and taking an excitation temperature of 1200 K , $^{12}\text{C}/^{13}\text{C} = 16$, in agreement with the photospheric absorption line value. Computing the isotopic ratio over the range of temperature uncertainties, an excitation temperature of 1000 K results in a carbon isotope ratio of 40, while 1400 K results in 10.

More than a dozen 1–0 lines from the $^{12}\text{C}^{18}\text{O}$ isotopologue could be identified. These lines are all weak emission features and heavily influenced by blending (see, for example, Figure 3). Taking these lines as upper limits, the $^{16}\text{O}/^{18}\text{O}$ ratio is $\gtrsim 70$. Only a few possible candidates for $^{12}\text{C}^{17}\text{O}$ 1–0 lines could be found. A set of random line positions produces a similar percentage of weak emission “lines,” implying that the lines detected were noise. We conclude that $^{12}\text{C}^{17}\text{O}$ emission lines are not present in the 2020 spectra. If the isotopic ratio is computed using the limiting C^{17}O intensities, $^{16}\text{O}/^{17}\text{O}$ has a value close to that found from the much more robust set of $^{12}\text{C}^{18}\text{O}$ 1–0 lines, implying that the $^{12}\text{C}^{18}\text{O}$ lines are also near the limit of detectability.

Table 2 contains a summary of the radial velocities for the M -band emission lines.

Table 2
Summary of M -band Emission Line Radial Velocities

Date	Molecule	Transition	RV ^a (km s^{-1})	Number of lines
1989 Jan 19	H_2O	011–010	-25.1 ± 1.2	2
2020 Aug 8	H_2O	011–010	-24.8 ± 0.7	7
2020 Aug 8	$^{12}\text{C}^{16}\text{O}$	3–2	-27.2 ± 0.6	7
2020 Aug 8	$^{12}\text{C}^{16}\text{O}$	2–1	-22.9 ± 0.3	14
2020 Aug 8	$^{12}\text{C}^{16}\text{O}$	1–0 P	-21.9 ± 0.5	10
2020 Aug 8	$^{12}\text{C}^{16}\text{O}$	1–0 R	-20.2 ± 0.4	7
2020 Sep 20	H_2O	011–010	-24.4 ± 0.4	9
2020 Sep 20	$^{12}\text{C}^{16}\text{O}$	3–2	-25.9 ± 0.4	7
2020 Sep 20	$^{12}\text{C}^{16}\text{O}$	2–1	-23.2 ± 0.3	16
2020 Sep 20	$^{12}\text{C}^{16}\text{O}$	1–0 P	-22.5 ± 0.4	12
2020 Sep 20	$^{12}\text{C}^{16}\text{O}$	1–0 R	-20.2	3

Note.

^a Heliocentric.

The eclipse of the R Aqr Mira is known to be partial, with the disk covering at most about 50% of the Mira (Whitelock et al. 1983). Mira absorption lines are indeed present in the spectrum during eclipse (Section 3.2). By using a reference Mira spectrum, the disk spectrum can be recovered. The single out-of-eclipse reference spectrum covers only the shorter-wavelength, $4.54\text{--}4.76 \mu\text{m}$ section of the M band. Of the groups of lines discussed, only the 2–1 lines are well represented in the out-of-eclipse reference spectrum. The 2–1 average in-eclipse line profile was ratioed, after correction for orbital motion, to the average out-of-eclipse line profile (Figure 7). The ratioed profile is double-peaked emission, the expected profile for lines originating across the surface of a disk (Smak 1981).

The out-of-eclipse reference spectrum also covers part of the 3–2 R branch. Three relatively unblended lines were found, R14, R15, and R23, in the out-of-eclipse spectrum. The in-eclipse average profile of these lines was ratioed to the average out-of-eclipse profile. This profile is single peaked with a radial velocity at the approximate midpoint of the 2–1 profile. Parameters for the ratioed lines can be found in Table 3.

3.3.2. H_2O

Emission lines from the 001–010, 010–000, and 100–010 vibration-rotation H_2O bands are present in the in-eclipse M -band spectrum. In general, there is no absorption associated with the H_2O emission lines. Oxygen-rich Miras have a rich H_2O absorption line spectrum, with the lines originating from both the upper photosphere and the cool stationary component (Hinkle & Barnes 1979). The absence of an absorption component in H_2O in-eclipse line profiles is unexpected. The in-eclipse H_2O emission peak is at -25.3 km s^{-1} . The emission is slightly asymmetric, with the more negative side broader. The FWHM of the average H_2O emission line is 8.9 km s^{-1} .

While most of the H_2O lines appear at the longer-wavelength end of the M band, there are a few lines in the 2150 cm^{-1} ($4.65 \mu\text{m}$) region where a reference out-of-eclipse spectrum exists. The 2144.808 cm^{-1} [001](220)–[010](221) and 2151.195 cm^{-1} [001](111)–[010](110) lines are in emission in the out-of-eclipse reference spectrum (Figure 3). The H_2O velocity out of eclipse is -26 km s^{-1} with a FWHM of 8.3 km s^{-1} . The orbital phase of the 1989 spectrum is 0.221 with the velocity of the WD predicted to be -19.2 km s^{-1} and

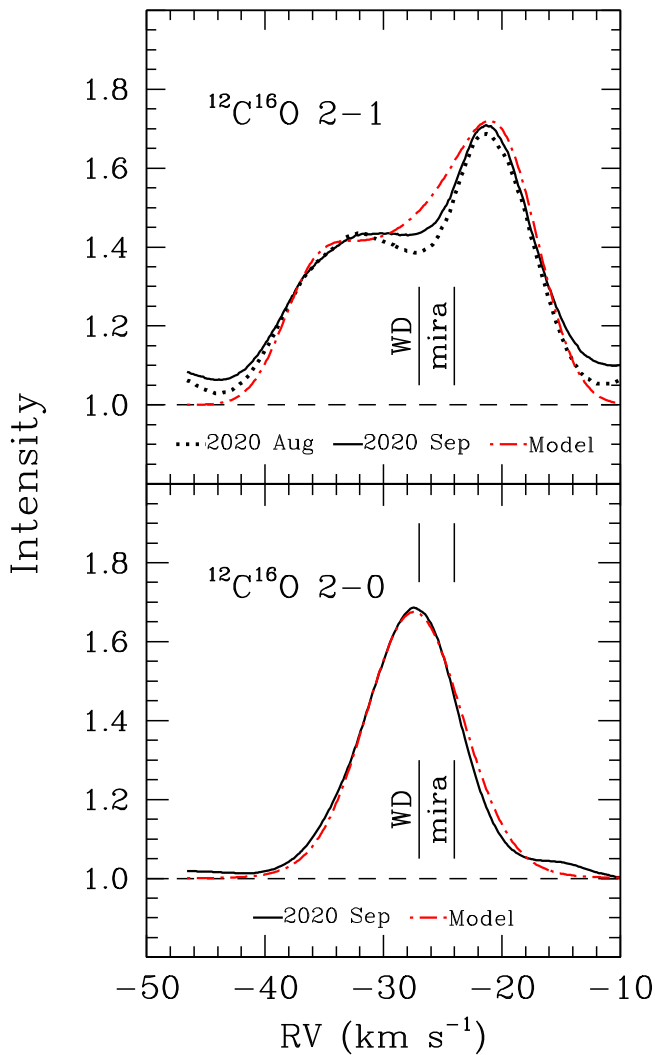


Figure 7. Upper panel: ratio (dotted line) of the in-eclipse average 2–1 line profile observed on 2020 August (panel (d) of Figure 4) to the out-of-eclipse profile observed on 1989 January (panel (c) of Figure 4). The solid line is the ratio for 2020 September. The velocities of the WD and Mira (vertical lines) are from the predicted orbit (Figure 1). Lower panel: ratio of the average 2–0 R branch line profile observed in eclipse on 2020 September (panel (b) of Figure 4) to the out-of-eclipse 1989 profile (panel (a) of Figure 4). Intensity units are relative to the local continuum. Model fits (see text) are the red dotted–dashed line.

Table 3
Ratioed Disk Emission Line Parameters

Transition	FWHM (km s^{-1})	FWZI (km s^{-1})	RV ^a (km s^{-1})	Comment
CO 2–0	9.1 ± 0.5	25.4 ± 0.5	-27.3 ± 0.5	Centrally peaked
CO 3–2	8.2 ± 0.5	20.0 ± 0.5	-27.4 ± 0.5	Centrally peaked
CO 2–1	18.8 ± 0.5	32.5 ± 0.5	-29.7 ± 0.2	Double-peaked asymmetric

Note.

^a Heliocentric.

the Mira -28.5 km s^{-1} (Figure 1). Thus, in the out-of-eclipse spectrum H_2O emission is associated with the Mira. The [001] (220)–[010](221) line also has absorption from both the photospheric and cool stationary layer. H_2O line profiles are expected to be highly phase dependent (Hinkle & Barnes 1979).

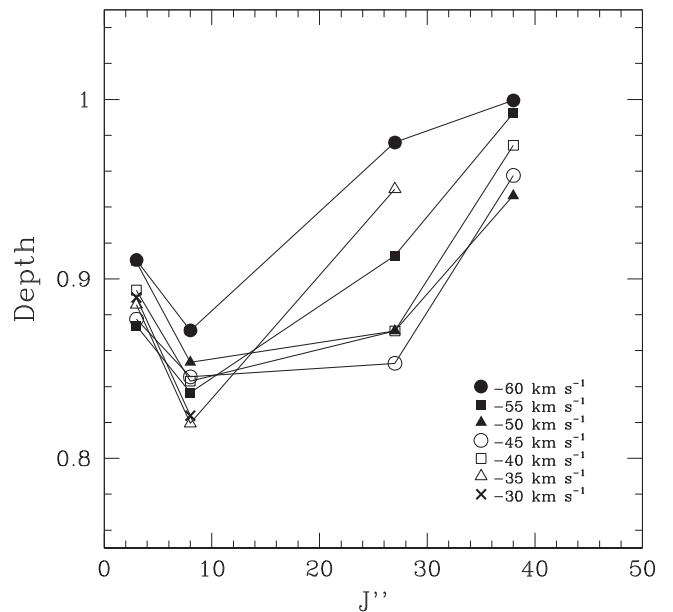


Figure 8. Depth of absorption as a function of J'' for the $^{12}\text{C}^{16}\text{O}$ 1–0 lines in the 2020 August in-eclipse spectrum measured at 5 km s^{-1} velocity steps across the line profile (see symbol key on figure). The lines used are R3, R8, the average of P22, 27, and 33 plotted at $J'' = 27$, and P38. The line profiles are shown in Figure 5, panels (a) and (b). The measurements at the same velocity for different J'' are connected by solid lines.

Since the two out-of-eclipse lines have different and unexpected line profiles, a more detailed analysis of in-eclipse H_2O is not possible at this time.

3.4. In-eclipse M-band Absorption Lines

The $^{12}\text{C}^{16}\text{O}$ 1–0 profiles have absorption blueshifted from the emission. For R3–8 the absorption starts at -23 km s^{-1} and extends to at least -60 km s^{-1} (Figure 5). The center-of-mass velocity for the Mira is $\sim -24 \text{ km s}^{-1}$ at the time of the observation, so the absorption is from gas flowing in the direction away from the Mira. For these lines the emission peaks at -20.5 km s^{-1} . The higher-excitation P21–41 lines show the absorption starting at $\sim -32 \text{ km s}^{-1}$ and continuing to $\sim -60 \text{ km s}^{-1}$ with the emission peaking at -22.3 km s^{-1} . Absorption related to the eclipse is not present in the 2–1 lines; the eclipse component of the 2–1 and 3–2 lines is entirely emission (Figure 7).

In Figure 8 the depth of the absorption every 5 km s^{-1} is plotted as a function of the rotational quantum number J'' for the 1–0 CO lines. The cleanest absorption line profiles are for 1–0 R3 and R8 and P22, 27, 32, 35, and 38. To increase the S/N, the depths of the P22, 27, and 32 lines were averaged and plotted at P27 in Figure 8. The depth as a function of J'' , while poorly sampled in J'' , peaks between $J'' \gtrsim 8$ and $J'' < 28$. The range of dust temperature, 550–1160 K (Omelian et al. 2020), corresponds to J_{max} in the range 9–14.

The absorption line profile consists of a number of velocity components (Figure 5). These have similar depths in the R3 and R8 lines but have a range of depths in P22–32. This does not necessarily reflect a range of excitation temperature. A model with a uniform gas temperature but different column densities for different velocity components fits the observations.

In late-type giant spectra, optical and near-IR atomic resonance lines and 1–0 low- J CO lines typically contain an

absorption component from the expanding circumstellar shell (Bernat et al. 1979). The circumstellar component has deep absorption and an excitation temperature near 200 K (Bernat 1981). Lines from an expanding circumstellar region are not present in the in-eclipse R Aqr spectrum (Panel (a) of Figure 5).

3.5. K band

In an analysis of the orbit based on near-IR *K*- and *H*-band spectra, Hinkle et al. (1989) found no spectral features in the *K* band that could be attributed to the secondary. While the data set employed is extensive, it does not include any eclipse observations. The absence of disk features in spectra observed outside of eclipse is not surprising since the out-of-eclipse SED in the 2.3 μm region arises from the Mira photosphere (Mayer et al. 2013). Photometry from the 1978 eclipse shows that the eclipse reduces the *K*-band flux by ~ 2.5 magnitudes (Jurkic & Kotnik-Karuzza 2018). The expectation is that features from the eclipse will be detectable in the spectra. The Mira flux and spectrum are strongly phase dependent, complicating an understanding of the eclipse-dependent effects. The out-of-eclipse *K*-band pulsation amplitude is ~ 0.81 magnitude (Whitelock et al. 2000).

Two sections of the *K*-band spectrum are presented in Figure 9, and the 2–0 line profile is shown in Figure 5. Approximately the same pulsation phases are compared in in-eclipse and out-of-eclipse data. The deepest spectral features in the 4200–4360 cm^{-1} (2.38–2.29 μm) region of the in-eclipse spectra, including the band heads, have central intensities of ~ 0.4 , with the intensity scale normalized to the continuum. In the out-of-eclipse spectrum the deepest features have intensity ~ 0.2 . A few atomic lines are shown in Figure 9. There are some tens of other isolated atomic lines in the less-blended region blue of the 2–0 CO bandhead. These lines, as well as the high-excitation CO lines, are about 80% of the out-of-eclipse depth in the in-eclipse spectra, similar to the weakening of the band heads. While the atomic lines and high-excitation CO lines are weaker in eclipse, the profiles are unchanged. These changes likely result from veiling due to the decrease of Mira flux relative to the disk flux.

The low-excitation CO lines are strikingly different between the in-eclipse and out-of-eclipse spectra (Figure 4). The intensity at the velocity of the Mira photosphere (Figure 4) is ~ 0.65 in eclipse and ~ 0.2 out of eclipse. The line profile looks like a blend of two absorption lines. After applying a shift for the orbital motion, average line profiles for the 2–0 low-*J* lines in 1989 January (out of eclipse) and 2020 August (in eclipse) were ratioed. The resulting profiles reveal that what appears in the observed spectrum as doubled absorption lines is, in fact, CO line emission filling in the Mira lines (Figure 7). The central velocity of the emission is -27.4 km s^{-1} with the emission spanning a FWHM of $\sim 10 \text{ km s}^{-1}$ and a full width at zero intensity (FWZI) of approximately twice this. The CO overtone emission is single peaked and at the approximate central velocity of the CO emission observed in the CO fundamental. The 2–0 line parameters measured from the ratioed profiles are summarized in Table 3.

4. Discussion: System Parameters

4.1. Orbit

StSy-D orbital periods are typically long, $\lesssim 1000$ yr (Kenyon et al. 1988). The 44 yr orbital period for R Aqr is among the shortest. Perhaps as a result of the corresponding close separation of the stellar components, the R Aqr system has a number of unusual features (Mayer et al. 2013), including a bipolar nebula that was ejected by a nova-like outburst ~ 600 yr ago (Mattei & Allen 1979; Liimets et al. 2018). From images of the bipolar nebula the inclination, *i*, of the disk, $\approx 72^\circ$, can be measured (Solf & Ulrich 1985). Yet more unusual (Whitelock 1987) is the bipolar jet associated with the system (Kafatos & Michalitsianos 1982). The jet forms an independent proof of the existence of the accretion disk around the WD (Melnikov et al. 2018).

Gromadzki & Mikołajewska (2009), Schmid et al. (2017), and Bujarrabal et al. (2018) combined optical, IR, and microwave radial-velocity measurements with microwave interferometry imaging to produce an orbit for the R Aqr Mira. The orbital period found is 43.6 ± 1.3 yr, with the orbit moderately eccentric, $e = 0.25 \pm 0.07$. While the uncertainty in the period is only 3%, this is more than a year, with corresponding uncertainty in predicting, for instance, times of periastron and conjunction. Predicted periastron is on JD 2459962 ± 471 , a calendar mid-date of 2023 January 17, with the predicted conjunction occurring before periastron by ~ 0.05 in phase, ~ 800 days, a calendar mid-date of 2020 November. Near-IR photometry reviewed in Section 2.2 indicates a mid-eclipse date of 2020 March.

The mass function, $f(m)$, from the orbital solution of Gromadzki & Mikołajewska (2009) is $0.096_{-0.032}^{+0.042}$. The mass function can be expressed as

$$f(m) = (m_{\text{wd}}^3 \sin^3 i) / (m_{\text{rg}} + m_{\text{wd}})^2,$$

where *i* is the orbital inclination, m_{wd} the WD mass, and m_{rg} the Mira mass. With a 72° inclination, Gromadzki & Mikołajewska (2009) suggest masses of 1.0–1.5 M_\odot and 0.57–1.02 M_\odot , respectively, for the Mira and WD with a Mira/WD mass ratio 1.2–2.1. The C and O isotopic abundances (Section 3.3.1) limit the main-sequence mass of the Mira to $< 1.5 M_\odot$ (Hinkle et al. 2016), in agreement with the Gromadzki & Mikołajewska (2009) mass.

From Kepler’s 3rd law, the semimajor axis for the system is 15.6 ± 1.6 au. However, with an eccentricity of 0.25, the periastron and apastron separations are significantly different. Interaction between the Mira, its circumstellar shell, the mass-transfer flow, and the WD accretion disk will vary over the course of the orbit. The periastron separation is ~ 11.7 au, with the Mira Roche radius¹⁰ ~ 4.9 au. At apastron the separation is ~ 19.5 au with the Roche radius ~ 8.2 au. The Roche radii for the WD are ~ 4.0 au and ~ 6.6 au at periastron and apastron, respectively. The photospheric (*J*-band) radius of the Mira is ~ 1.4 au (Woodruff et al. 2009) to 2.4 au (Millan-Gabet et al. 2005) so the system is detached even at periastron.

¹⁰ The Roche-lobe radius is approximated by the volume radius (Eggleton 1983) unless otherwise specified.

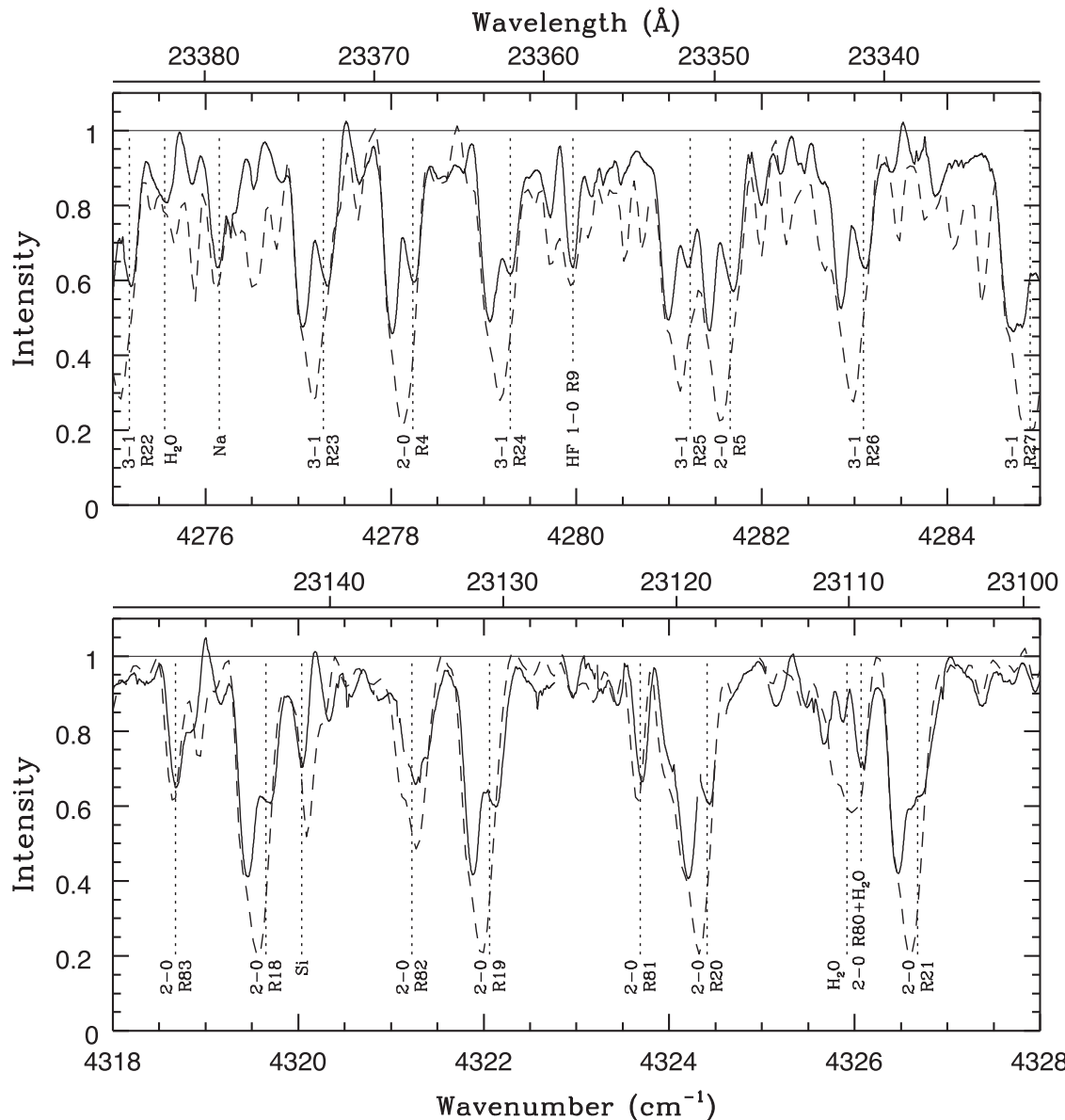


Figure 9. Two sections from *K*-band spectra of R Aqr. The dashed line is an out-of-eclipse 1989 spectrum. The solid line is the in-eclipse 2020 September spectrum. The spectra are shifted so the atomic lines appear at the rest frequency. The telluric spectrum has been removed by ratioing to synthetic reference spectra. $^{12}\text{C}^{16}\text{O}$ 2-0 and 3-1 lines are labeled. Large changes in the low-*J* lines (Figure 4) are apparent. For the other lines, for instance Na 4276 cm^{-1} (top panel) and CO R83 and R81 (bottom panel), the in-eclipse lines are slightly less deep than the out-of-eclipse lines. To compare the scale of the abscissa to the line profiles to Figure 4, broad lines, for example 2-0 R4 and 2-0 R19, have widths of $\sim 0.5 \text{ cm}^{-1}$ corresponding to 35 km s^{-1} .

4.2. Mira Mass Loss

The Mira primary in the R Aqr system is oxygen-rich (M6–9; Keenan et al. 1974) with a pulsation period of 387–390 days (Mattei & Allen 1979), a luminosity of $\sim 7000 L_{\odot}$ (Mayer et al. 2013), and, averaged over the light cycle, an effective temperature of $\sim 2800 \text{ K}$ (Contini & Formigginì 2003), typical values for field Miras (Whitelock et al. 2008). The R Aqr circumstellar shell is truncated by the Roche lobe, depending on orbital phase, at 4.9 au to 8.2 au. The truncated radius of the circumstellar shell is confirmed by the circumstellar masers. SiO masers are formed at $\sim 4.5 \text{ au}$ (Assaf 2018) and are present in the R Aqr microwave spectrum (Min et al. 2014). Characteristic radii for the formation of H_2O and OH masers are 11 au (Menten et al. 2008) and 110 au (Chapman et al. 1994). H_2O maser lines are seen in the spectrum of R Aqr but with abnormal strengths, suggesting the R Aqr H_2O maser

forms close to the star (Iverson et al. 1998). No OH masers are seen (Bujarrabal et al. 2010).

Silicate dust formation occurs in the circumstellar shell of oxygen-rich Miras at $\sim 24 \text{ au}$ and is an important driver of mass loss (Perrin et al. 2015). This places the formation of silicate dust outside the Roche limit in R Aqr. However, the R Aqr mid-IR spectrum contains amorphous silicate features at 9.7 and $18 \mu\text{m}$, corresponding to a mass-loss rate of $7 \times 10^{-7} M_{\odot} \text{ yr}^{-1}$. This includes material trapped in the binary and sets an upper limit for the Mira mass-loss rate (Mayer et al. 2013).

Circumstellar microwave CO lines are detected in R Aqr. The mass-loss rate determined from microwave CO is typical for an oxygen-rich Mira (see, for example, Knapp & Morris 1985), $2.7 \times 10^{-7} M_{\odot} \text{ yr}^{-1}$ (Hollis et al. 1985), and variable (Ramstedt et al. 2018). The CO also sets the circumstellar outflow velocity, $10\text{--}15 \text{ km s}^{-1}$ (Ramstedt et al.

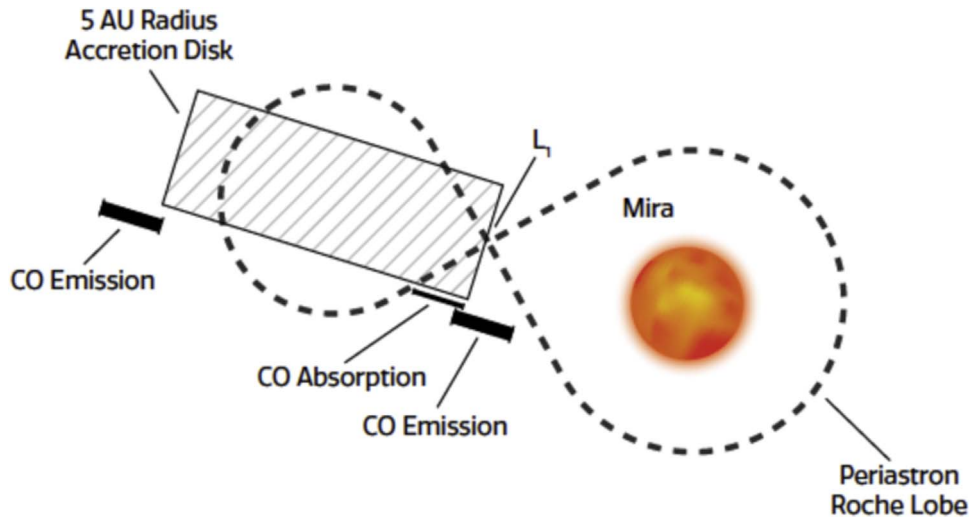


Figure 10. Graphic of the R Aqr system near mid-eclipse viewed from the side. The system is inclined 18° to the line of sight. The hatched rectangle is the nominal 5 au radius accretion disk with $h/r = 0.2$. The orange disk labeled “Mira” illustrates the approximate 2 au radius of the Mira’s IR photosphere. The approximate shape of the Roche potential is illustrated using the Eggleton (1983) radius (heavy dashed line). The potential is shown extended to the inner Lagrange point, L_1 . The Roche radius of the Mira at periastron is ~ 4.9 au and of the WD ~ 4.0 au. L_1 is ~ 6.4 au from the center of the Mira (Plavec & Kratochvil 1964) and the Mira is clearly detached. Eclipse is near periastron when the WD Roche lobe is smaller than the *nominal* accretion disk. At apastron the WD Roche radius is ~ 6.6 au. The approximate regions observed in CO emission and absorption are marked.

2018; Bujarrabal et al. 2018), a typical value for a cool, oxygen-rich Mira (Knapp & Morris 1985). As noted in Section 3.4, the corresponding Mira circumstellar spectral features are not present in the IR during eclipse, confirming the spatial and/or temporal complexity of the circumstellar region.

4.3. Disk Parameters

The Bondi–Hoyle–Littleton (BHL) models of Perets & Kenyon (2013) give an accretion disk radius of ~ 5 au. The relations in Ireland et al. (2007) for combining orbital and wind velocities similarly give a BHL accretion radius of ~ 5 – 7 au. Limits on the size of the disk also can be placed using orbital parameters. The WD and Mira have relative velocities of $\sim 12 \text{ km s}^{-1}$ at the time of the eclipse. An eclipsing body of 10 au length will take ~ 4 yr to pass in front of the Mira. The maximum possible eclipse duration of 8.5 yr (Willson et al. 1981) limits the overall size of the obscuring disk and mass flow to ~ 21 au.

The IR excess measured by the Infrared Astronomical Satellite (IRAS) for R Aqr, and for other SySt-D, can be fit by a two-temperature model (Anandarao & Pottasch 1986; Anandarao et al. 1988), a relatively compact 800 K region and a much larger ~ 80 K region. The 80 K region is the extended region of mass lost from the system (see, for instance, Gehrz et al. 2015). Danchi et al. (1994) found the compact region dust temperature to vary with Mira phase, ~ 830 K at Mira maximum and ~ 530 K at minimum. Jurkic & Kotnik-Karuza (2018) found that time-series near-IR photometry gives a mean disk dust temperature of $\sim 650 \pm 50$ K. Mid-IR photometry observed with the Stratospheric Observatory for Infrared Astronomy (SOFIA) Faint Object infraRed CAmera for the SOFIA Telescope (FORCAST) and analyzed along with ISO Short Wavelength Spectrometer data are best fit by $3 \mu\text{m}$ diameter silicate grains having temperatures covering the range 550–1160 K (Omelian et al. 2020). The $12.2 \mu\text{m}$ flux is a function of both orbital phase and pulsation phase, with the orbital minimum temperature occurring near conjunction. Omelian et al. (2020) note that the hot dust temperature

overlaps temperatures at which silicates condense (Höfner 2007; Gobrecht et al. 2016).

Radiation is likely the principal disk-heating mechanism in R Aqr and, hence, confined to the side facing the giant/supergiant (Stencel et al. 2011). As the separation of the two stars in R Aqr varies during the orbit from 11.7 to 19.5 au and, assuming a 5 au accretion disk radius and 2 au Mira radius, the distance from the disk edge to the Mira changes from ~ 4.7 au to 12.5 au. By employing the relation of Ragland et al. (2008) for totally absorbing grains, the upper-limit temperature for radiatively heated grains varies from 800–1250 K over the course of the orbit, similar to the 550–1160 K range reported by Omelian et al. (2020). Similarly, the range of temperatures observed in the ϵ Aur disk is ~ 1150 K for the star side of the disk and ~ 550 K for the shaded side (Hoard et al. 2012; Pearson & Stencel 2015). Since the disk comes between the Mira and the observer during eclipse, the shaded side is toward the observer, in agreement with the $12.2 \mu\text{m}$ flux minimum measured near periastron (Omelian et al. 2020). At Mira maximum light closest to periastron the temperature of the disk on the Mira-facing edge is highest. Disk rotation carries the heated dust toward the trailing edge.

The basic shape and size of the disk can be constrained by geometry since both the inclination is known and the separation of the components is known from the spectroscopic orbit.¹¹ The eclipsing disk is known to be optically thick from near-IR photometry (Whitelock et al. 1983) and the structure of the expanding bipolar shells (Solf & Ulrich 1985). The ϵ Aur disk is also optically thick (Kloppenborg et al. 2010; Pearson & Stencel 2015). The R Aqr disk is inclined 72° and, at

¹¹ The distance to R Aqr is not required for this calculation. This is fortunate since distance estimates range over about a factor of 2. A kinematic distance, 260 pc, was found from the nebular expansion by Gregory & Seaquist (1974) and revised to 178 ± 18 pc by Liimets et al. (2018). Very long baseline interferometry (VLBI) observations of SiO maser spots gives 218_{-11}^{+12} pc (Min et al. 2014). The European Space Agency Gaia mission Data Release 2 (Bailer-Jones et al. 2018) distance is 320_{-26}^{+31} pc. Discussion on reconciling VLBI and Gaia parallaxes is given by Xu et al. (2019). The Mira period–luminosity relation distance is 250 pc (Whitelock et al. 2008).

conjunction, 12 au from a Mira of diameter 4 au. If the disk radius is assumed to be 5 au, geometry requires an outer -edge disk height of ~ 1 au for a 50% eclipse, as sketched in a graphic (Figure 10), where the disk height defines the occulting edge. The disk scale height ratio (h/r) in the cartoon is 0.2. Michalitsianos et al. (1988) argued that a thick disk is required to form the R Aqr jet. For comparison, the ϵ Aur eclipsing disk has a radius (r) of ~ 3.8 au and a height (h) of ~ 0.8 au, i.e., $h/r \sim 0.2$ (Kloppenborg et al. 2010). Clearly, Figure 10 is highly schematic. The shape and orientation of the disk are more complex, as shown by models of the mass exchange (Section 4.4). Early models of the R Aqr system by Theuns & Jorissen (1993) predict a tipped disk.

Again, the ϵ Aur disk can provide a comparison. The gas content of the ϵ Aur disk is not symmetric about the central B main-sequence star. The trailing edge has approximately twice the gas density of the leading edge (Muthumariappan et al. 2014). Unequal radial-velocity amplitudes between ingress and egress, first noted by Struve et al. (1958), require that the disk is elliptical in the direction of the orbital motion (Strassmeier et al. 2014). CO first overtone lines have been observed only after mid-eclipse. Stencel et al. (2011) attributes this to sublimation of disk grains. During the second half of the eclipse, CO absorption occurs over an ~ 1 au path along a chord that transects part of the disk edge. The column density along this chord is $\sim 10^{20} \text{ cm}^{-2}$, implying $n_{\text{H}} \sim 3 \times 10^{10} \text{ cm}^{-3}$ with the CO at an excitation temperature of ~ 1000 K (Stencel et al. 2015). Pearson & Stencel (2015) propose $h/r = 0.2$ at the edge but flared with a central $h/r = 0.05$.

Near periastron the R Aqr secondary Roche radius decreases to ~ 4.0 au (Section 4.1), less than typical values for the disk radius. As illustrated by a graphic (Figure 10), a disk of radius ~ 5 au is required by the photometry for the eclipse to cover half the Mira. However, while this disk fits in the secondary to inner Lagrange point (L_1) radius (Plavec & Kratochvil 1964), it significantly exceeds the Roche radius (Figure 11). Modeling beyond the scope of this paper is required to explore the three-dimensional nature of the accretion disk and eclipsing body. In any case, the outer parts of the disk, as well as the mass-transfer stream, will be disrupted by the contraction of the Roche lobe near periastron in each 44 yr orbital cycle.

4.4. Literature Disk Models

Mass flow onto a WD companion has been extensively studied in cataclysmic variables, systems that contain a WD and a cool dwarf star (Warner 1995). Dominant features of the mass transfer in cataclysmics are a circum-WD disk (e.g., Buckley & Tuohy 1989) and a hot spot where mass transfer collides with and penetrates the disk (Bath et al. 1983). The accretion flow in these systems is close to Keplerian. However, as noted by Lee et al. (2022), SySt accretion involves the capture of slow stellar wind from a giant donor and is different from that in geometrically thin, cataclysmic, variable accretion disks.

Accretion disk models for SySt-D systems have been discussed by de Val-Borro et al. (2009, 2017) based on wind Roche-lobe overflow (WRLOF; Mohamed & Podsiadlowski 2007). WRLOF circumstellar flows are highly aspherical and focused toward the binary orbital plane (Mohamed & Podsiadlowski 2012). Both BHL and WRLOF models applicable to R Aqr show complex circumstellar structure (Nagae et al. 2004) with hydrodynamic simulations

showing spiral mass flows (Liu et al. 2017; Chen et al. 2017; Saladino et al. 2019). Simulations of Roche-lobe overflow show that the flow forms an elliptical accretion disk around the WD. Viewed so the orbital motion of the WD is clockwise around the Mira, the disk rotation is clockwise. Acceleration by both gravity and the Coriolis force results in a supersonic flow that penetrates into the disk, creating a hot spot. The long axis of the disk is aligned roughly with the orbit, with the hot spot on the trailing edge.

A WRLOF prediction of particular interest to R Aqr is that the formation of the accretion disk depends of the ratio of the AGB terminal wind velocity to the orbital velocity. For systems with terminal wind velocities larger than the orbital velocity, the models do not predict a large accretion disk (Saladino et al. 2018). Due to the eccentricity of the R Aqr orbit, the orbital velocity changes from 13 km s^{-1} at periastron to 10 km s^{-1} at apastron. The terminal wind velocity is in the range $10\text{--}15 \text{ km s}^{-1}$ (Bujarrabal et al. 2010; Ramstedt et al. 2018). The wind velocity is in the range where enhanced mass transfer to the accretion disk is possible near periastron.

5. Discussion: The 2020 Eclipse

Additional constraints on the disk can be derived from diagnostic signatures in the $2\text{--}5 \mu\text{m}$ region spectra observed during eclipse: emission in low-excitation CO $\Delta v = 1$ and $\Delta v = 2$ lines, very shallow absorption in low-excitation CO $\Delta v = 1$ lines, and continuum emission in the M and K bands.

5.1. CO Emission

5.1.1. Summary of Observations

During the eclipse an emission component is present in lower-excitation lines of both the CO vibration-rotation fundamental (Section 3.3) and the first overtone (Section 3.5).

There are three fundamental vibration-rotation bands in emission. The 1–0 lines have an emission component but, due to lack of out-of-eclipse reference spectra, the shape of the profile is not known. The profile of the 2–1 CO emission lines, extracted by ratioing to out-of-eclipse lines, is double peaked and asymmetric (Figure 7). The profile of the 3–2 CO emission lines is centrally peaked with approximately half the FWHM of the 2–1 profile and a velocity near the center of the double-peaked 2–1 lines.

The first overtone, low-excitation 2–0 and 3–1 CO lines contain an emission component. By ratioing the line profiles to a reference out-of-eclipse profile, a centrally peaked profile was extracted (Figure 7). The line profile is nearly the same as that of the fundamental band 3–2 lines. Overtone emission implies that the fundamental is optically thick, since the fundamental is the preferred route.

Parameters for the CO emission lines are listed in Table 3.

5.1.2. Modeling

Assuming a model R Aqr disk of 5 au radius centered on a $0.7 M_{\odot}$ WD, the gas at the outer edge of the disk has a projected Keplerian velocity of $\sim \pm 11 \text{ km s}^{-1}$. Spectral lines originating in a rotating disk are double peaked (Smak 1981; Horne & Marsh 1986). Using the above parameters and convolving the output to the spectral resolution of iSHELL ($R \sim 3.4 \text{ km s}^{-1}$), the synthesized double-peaked profiles are

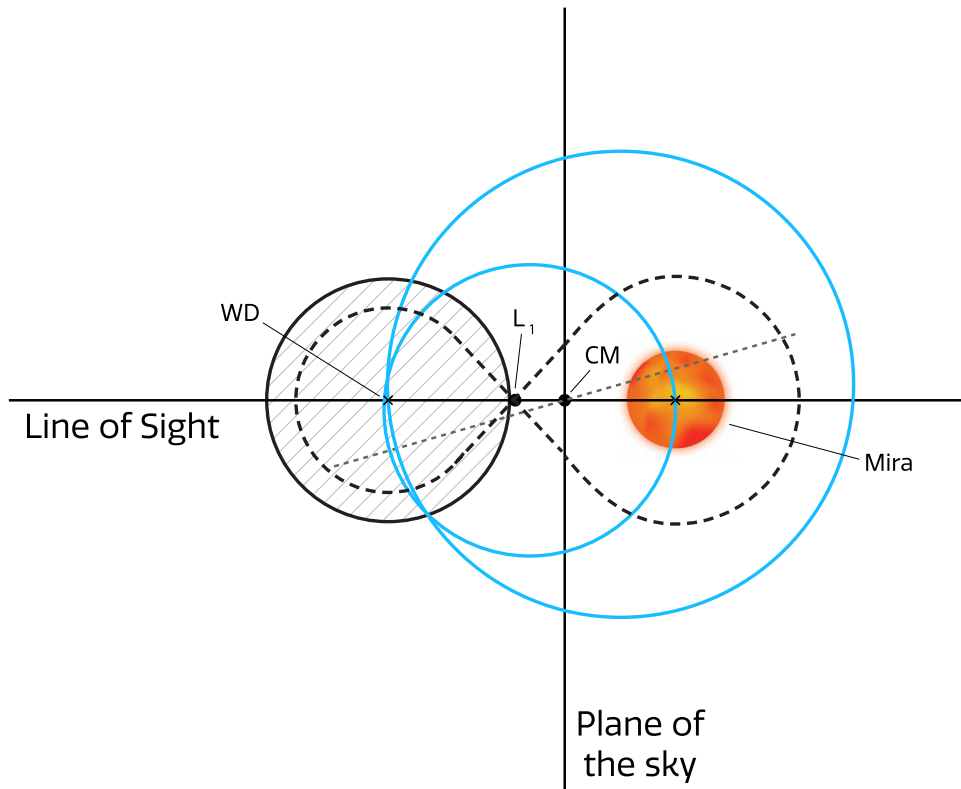


Figure 11. Graphic of the R Aqr system near mid-eclipse viewed perpendicular to the plane of the orbit. The orbits for the WD and the Mira are shown by the blue circles. The orbital direction in this view is clockwise. The line marked “Plane of the sky” is an intersection of the plane of the sky with the plane of the orbit. CM is the center of mass, and L_1 is the inner Lagrange point. The light, short-dashed line is the line of apsides. The WD, Mira, and associated Roche lobes (Figure 10) are shown at mid-eclipse. The hatched circle is a 5 au radius accretion disk.

well resolved and readily detectable. The observed 2–0 and 3–2 CO lines are single peaked and more narrow than the disk synthetic profile. In order to produce this profile the 2–0 and 3–2 lines must originate at a bright spot on the disk. Fits of the observed profile indicated that the emission falls off rapidly with radius (r) or it would be broadened by disk rotation. A r^{-6} decline was adopted.

Since the brighter side of the 2–1 line profile is offset from the centrally peaked 2–0 and 3–2 line profiles, the 2–1 CO profile does not result from an emitting bright spot superimposed on a double-peaked disk profile. One way to account for the asymmetric line profile is an eccentric disk around the WD. The brighter side of the 2–1 profile is redshifted. Wind accretion models predict an eccentric disk that bulges on the opposite side from the accretion flow (Section 4.4). The eccentric bulge, viewed at mid-eclipse, would be redshifted due to the disk rotation (de Val-Borro et al. 2009).

We fit the line profiles by integrating over the disk and assuming the gas is in a Keplerian orbit around the WD. For the overtone emission a model with a circular disk having a bright spot is sufficient. For the 2–1 fundamental emission the disk must be eccentric. This requires that the eccentricity of the orbit for the disk gas declines with radius as

$$e(r) = e_0 \left(\frac{r}{R_{\text{in}}} \right)^\alpha$$

and the intensity of the disk varied as

$$I(r) = I_0 \left(\frac{r}{R_{\text{in}}} \right)^\beta.$$

Table 4
Accretion Disk Model

Parameter	Fundamental Value	Overtone Value
e_0	0.301	0.0
R_{in}	4.75 au	1 au
R_{out}	6.90 au	6.3 au
α	−3.04	...
β	−2.68	−5.9
Intrinsic line width	2.016 km s ^{−1}	3.29 km s ^{−1}
Doppler shift	−29.7 km s ^{−1}	−25 km s ^{−1}

We varied e_0 , R_{in} , R_{out} , α , β , the intrinsic line width, and Doppler shift of the line. The intensity scale of the profile is arbitrary so I_0 is a scaling factor. To estimate the error bars on the line profile we measured the standard deviation of the difference between the line profiles constructed from the data acquired in August and in September. The disk was assumed to be tipped 72° with a central $0.7 M_\odot$ object that did not contribute flux. The best fits are presented in Figure 7. The reduced $\chi^2 = 1.4$. The parameters that produced the best fits are presented in Table 4. A face-on view of the modeled disk for the CO overtone is shown in Figure 12 and for the CO fundamental in Figure 13. The area of the 2–1-emitting region in the model is $\sim 79 \text{ au}^2$.

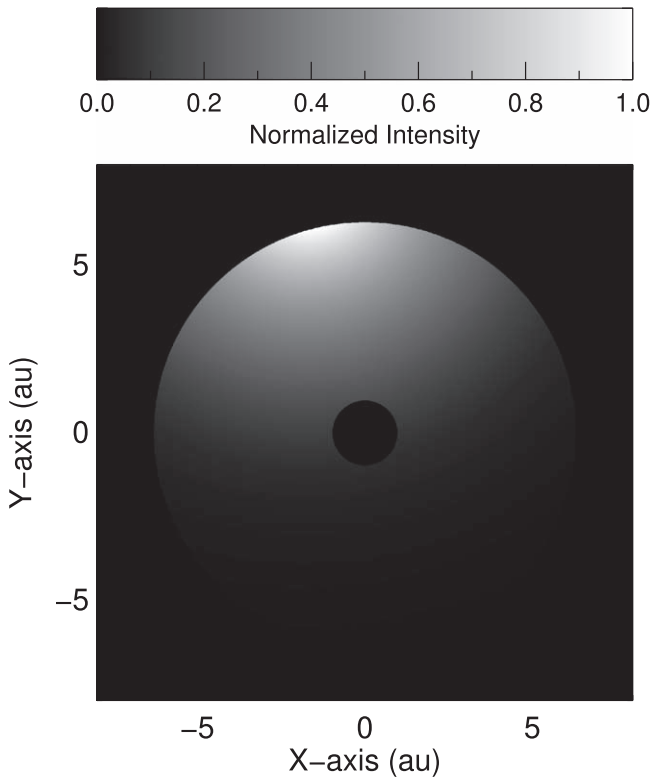


Figure 12. Model disk for the CO first overtone emission seen face-on. The semimajor axis is oriented to the top. The disk is moving to the right.

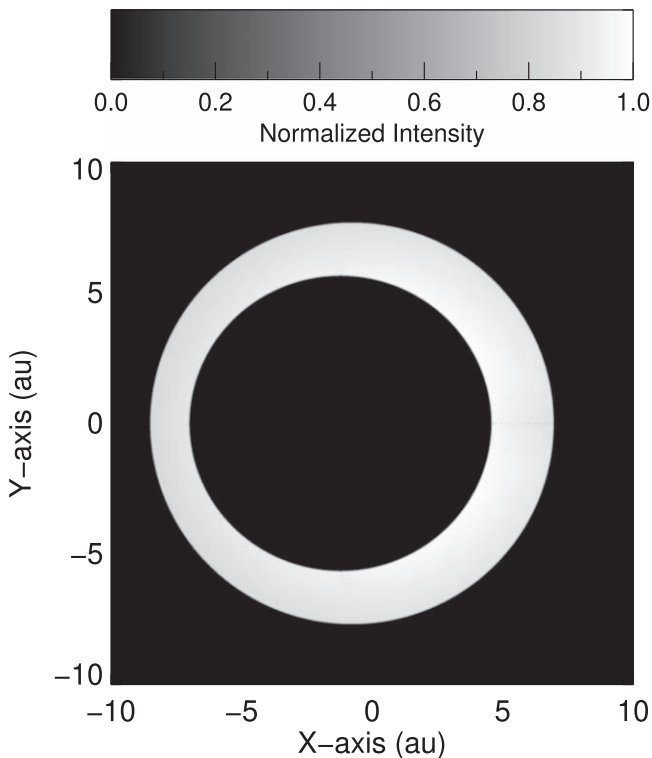


Figure 13. Model disk for the CO 2-1 emission seen face-on.

5.1.3. Disk Extent

The derived inner and outer radius of the emitting region, $R_{\text{in}} = 4.75$ au and $R_{\text{out}} = 6.9$ au, fall outside of the 4.0 au secondary Roche radius at periastron (Section 4.1). Nonetheless, these regions can be modeled by Keplerian rotation. The dust that is no longer in the Roche lobe moves outward on a tangential velocity vector, and a shock results where the expanding ring encounters the cold, 80 K (Section 4.3) circumbinary gas.

The CO excitation temperature is ~ 1200 K (Section 3.3). For this excitation temperature the equivalent widths of the emission lines correspond to an emission measure, $n(\text{CO})V_{\text{sh}}$, of $\sim 2 \times 10^{44}$ molecules, where V_{sh} is the volume of the shell seen in emission. The assumption has been made that the emission is optically thin, hence this is a lower limit. Assuming $N(\text{C})/N(\text{H}) \sim 10^{-4}$ and complete association of C into CO, the corresponding total mass of the CO-emitting region is $\gtrsim 10^{-8} M_{\odot}$. From microwave CO lines, Bujarrabal et al. (2010) find a circumstellar density of 3×10^8 to 10^9 cm^{-3} . Combining this with the emission measure, the volume of the emitting region is at least a cubic au. Dividing the volume by the $\sim 79 \text{ au}^2$ area of the emission region, the thickness of a uniform emitting region is $\gtrsim 6 \times 10^5 \text{ km}$ ($4 \times 10^{-3} \text{ au}$).

The CO fundamental emission lines have a well-defined gradient of radial velocity with excitation energy (Figure 6). The lowest excitation lines have a central peak that is redshifted. With higher energy the peak moves to a velocity close to that of the WD center of mass. The velocity gradient indicates that a range of profiles exists, ranging from double peaked, with enhanced emission on the red side, to single peaked. The highest excitation lines are observed $\sim 2 \text{ km s}^{-1}$ negative of the binary systemic velocity. This is in agreement with the emission occurring near the L_1 point from mass flowing away from the Mira (Figure 10). The 1200 K CO excitation temperature is near the grain-dissociation temperature in accord with the expected temperature near L_1 at periastron (Section 4.3).

5.2. CO Absorption

Absorption in the 1-0 CO lines is at velocities spanning the range $+4$ to -33 km s^{-1} relative to the WD velocity (Section 3.4). The low-velocity section of the 1-0 profile is contaminated by the Mira line profile; no reference out-of-eclipse spectrum exists for these lines. However, the more blueshifted lines are well beyond the width of the Mira line profile (Figure 5). Since the lines are in absorption, the CO is seen against a continuum. The shallow lines required a continuum temperature near the gas temperature, implying the continuum is the disk, not the Mira. The WD and Mira velocities are similar at the time of the observations. Thus, the blueshifted absorption is from gas flowing away from the Mira. A likely origin for the gas is heating of grains at the disk edge facing the Mira (Figure 10). In this case, the gas flow is toward the cooler interior of the disk.

The 1-0 CO absorption is $\sim 15\%$ below the continuum for the strongest features (Figure 5). This would be the case if the temperatures of the absorbing gas and the continuum-forming region are not that different. For instance, by assuming a dust continuum temperature of 800 K (Section 4.3) and an isothermal absorbing region, a CO excitation temperature only 30 K lower, 770 K, is required for lines of depth 15% below the

continuum. The nondetection of absorption in the 2–1 lines provides a limit to the column density of $\sim 10^{18} \text{ cm}^{-2}$, assuming an excitation temperature of 770 K and a microturbulence of 5 km s^{-1} . Assuming $N(\text{C})/N(\text{H}) \sim 10^{-4}$ and complete association of C into CO, the column density of hydrogen is $\sim 10^{22} \text{ cm}^{-2}$. Applying the Bujarrabal et al. (2010) circumstellar density of 3×10^8 to 10^9 cm^{-3} , the path length is in the range 0.7–2 au.

The disk-eclipse F supergiant ϵ Aur has similar dimensions, a ~ 1 au path length observed in CO and a 10 au diameter disk (Stencel et al. 2015). In the case of ϵ Aur the CO absorption has been interpreted as gas along the line of sight through a cold disk edge to the stellar photosphere. Similar path lengths may be indicative of the path length over the disk edge before CO is reabsorbed into the grains.

5.3. Continuum

The variability of the Mira complicates understanding the disk and photospheric contributions to the flux. The Mira has a radius of ~ 2 au, $\sim 40\%$ of the disk radius (Figure 10). Seen face-on the stellar surface area is about 16% of the disk area. Assuming a h/r of 0.2 and a 72° inclination, the projected area of the disk is about 42% of the face-on value, i.e., the stellar surface area is about 38% of the disk surface area. Since the flux is a power-law function of the temperature and the stellar photosphere is at least twice as hot as the disk, the flux from the star is ~ 10 times that from the disk at $2.25 \mu\text{m}$ and 4 times at $5 \mu\text{m}$. Thus, it is not surprising that the disk contribution is not obvious out of eclipse. However, with the star half covered during eclipse, the contribution of the disk continuum is easily detected in the M band.

6. Summary and Conclusions

Near-IR, M -band, and K -band spectra are used to investigate the eclipse of the R Aqr system. A variety of eclipse-related emission and absorption features are present and their relationship to the disk is explored. R Aqr has long been known to be a dusty, symbiotic Mira plus WD binary (SySt-D). The R Aqr orbital period is $43.6 \pm 1.3 \text{ yr}$ (Gromadzki & Mikolajewska 2009) with an opaque body (Whitelock et al. 1983) eclipsing the Mira for $\lesssim 8.5 \text{ yr}$ (Willson et al. 1981). These parameters place R Aqr in the disk-eclipse family of giants and supergiants, long-orbital-period binary systems where mass transfer is taking place to a dusty disk of several au radius. In R Aqr, as in other members of this family, the disk is an obvious feature of the binary only during an eclipse (Hajduk et al. 2008). The orbital eccentricity, $e = 0.25$, of the R Aqr orbit is shown to play a key role in this system.

Published J -band photometry of R Aqr (Jurkic & Kotnik-Karuzza 2018) combined with recent I -band AAVSO photometry shows that mid-eclipse occurred in mid-2020. High-resolution spectra of the R Aqr M -band $4.5\text{--}5.5 \mu\text{m}$ region and K -band $2.2\text{--}2.4 \mu\text{m}$ regions were observed in 2020 August and September, near the time of mid-eclipse.

Multiwavelength data in the literature and models of mass transfer in Mira–WD systems are combined with modeling of the IR line profiles. From the orbit it is known that the primary does not fill its Roche lobe. As a result of the orbital eccentricity, the disk edge to Mira surface separation ranges from 4.7 to 12.5 au over the course of the orbit. Conjunction is near the time of periastron. The temperature of the disk

observed varies from 550 to 1160 K during the orbit. Near periastron the disk temperature on the Mira-facing side reaches maximum, in the range required for grain destruction.

The M -band spectra observed at mid-eclipse are complex. The spectrum of the Mira is present but weakened due to obscuration and continuum veiling by the disk. The lower-excitation $4.5\text{--}5.5 \mu\text{m}$ CO fundamental lines contain an emission component. The excitation temperature of the CO emission is $\sim 1200 \text{ K}$. Fits to the 2–1 line profile show that the emission originates in an eccentric ring around the secondary with inner radius $\sim 4.75 \text{ au}$ and outer radius $\sim 6.9 \text{ au}$. The higher-excitation 3–2 lines and emission in the low-excitation first overtone CO lines is shown to originate from a bright spot on the Mira-facing edge, $\sim 6.3 \text{ au}$ from the disk center. This bright spot is near L_1 . The peak velocity of the line profiles as a function of excitation shows a smooth transformation between these emitting regions. This suggests a three-dimensional shape for the emitting region, perhaps aligned with the Roche potential. The emitting region corresponds to a layer of thickness $\gtrsim 4 \times 10^{-3} \text{ au}$.

Previous observations and models for the accretion disk in the R Aqr system indicate a radius of $\sim 5 \text{ au}$. The outer radius of the emitting ring seen in CO is nearly 2 au larger. The Roche radii undergo $\pm 25\%$ changes due to the orbital eccentricity. At apastron a disk of 5 au radius easily fits in the secondary Roche radius of $\sim 6.6 \text{ au}$. At periastron the Roche radius of the secondary is $\sim 4.0 \text{ au}$, smaller than the outer edge of the posited 5 au radius accretion disk. The CO-emitting ring is nearly all at radii larger than the Roche lobe and must not be gravitationally bound to the secondary. Dust beyond the Roche limit will expand about 0.5 au yr^{-1} due to the tangential velocity after the shrinking Roche radius becomes smaller than the local radius of the disk. The CO emission region is estimated to be $\gtrsim 4 \times 10^{-3} \text{ au}$ thick. A likely origin is the zone where the expanding ring encounters circumbinary material.

Deep, narrow CO lines formed in an expanding circumstellar shell are absent from the eclipse spectrum, in accord with the Mira circumstellar shell being terminated near periastron by the Roche lobe. During eclipse shallow, blueshifted absorption appears in the lowest excitation CO lines. The absorption has an excitation temperature close to that of the dust continuum. Adopting a typical literature value for the dust continuum, 800 K, the CO excitation temperature is $\sim 770 \text{ K}$ with multiple velocity components along the line of sight. The CO is flowing away from the direction of the Mira in streams with velocities, relative to the disk center, up to 34 km s^{-1} . The CO absorption has a column density of $\sim 10^{18} \text{ cm}^{-2}$ and a path length of $\sim 0.7\text{--}2 \text{ au}$. Similar CO absorption is seen in other disk-eclipse systems, suggesting that the flow is related to recycling of material through the disk.

We thank the anonymous referee for comments that greatly improved the readability of this paper. Sharon Hunt provided assistance with the references. Peter Marenfeld prepared the graphics for Figures 10 and 11. We acknowledge with thanks the variable star observations from the AAVSO International Database contributed by observers worldwide and used in this research. This research was facilitated by the Set of Identifications, Measurements and Bibliography for Astronomical Data basebase (SIMBAD), operated by the Centre de données astronomiques de Strasbourg (CDS) in Strasbourg, France, and NASA’s Astrophysics Data System Abstract Service. The SM

plot, developed by Robert Lupton and Patricia Monger, was used in the production of some figures. This work made use of data from the European Space Agency (ESA) mission Gaia (<https://www.cosmos.esa.int/gaia>), processed by the Gaia Data Processing and Analysis Consortium (DPAC). Funding for the DPAC has been provided by national institutions, in particular the institutions participating in the Gaia Multilateral Agreement. The National Science Foundation (NSF) National Optical-Infrared Astronomy Research Laboratory NOIRLab is operated by the Association of Universities for Research in Astronomy (AURA) under cooperative agreement with the NSF. K.H. expresses thanks to the NOIRLab Research and Science Services (RSS) division for support of this research. The research at Tennessee State University was supported in part by the State of Tennessee through its Centers of Excellence program. This research used data obtained at the Infrared Telescope Facility, which is operated by the University of Hawaii under contract 80HQTR19D0030 with NASA. This project was supported in part by Universities Space Research Association (USRA) SOFIA grant No. 07-0014 to AURA.

ORCID iDs

Kenneth H. Hinkle  <https://orcid.org/0000-0002-2726-4247>
 Sean Brittain  <https://orcid.org/0000-0001-5638-1330>
 Francis C. Fekel  <https://orcid.org/0000-0002-9413-3896>
 Thomas Lebzelter  <https://orcid.org/0000-0002-0702-7551>
 Adwin Boogert  <https://orcid.org/0000-0001-9344-0096>

References

- Allen, D. A. 1984, *PASA*, **5**, 369
 Anandarao, B. G., & Pottasch, S. R. 1986, *A&A*, **162**, 167
 Anandarao, B. G., Taylor, A. R., & Pottasch, S. R. 1988, *A&A*, **203**, 361
 Assaf, K. A. 2018, *ApJ*, **869**, 80
 Bailer-Jones, C. A. L., Rybizki, J., Fouesneau, M., et al. 2018, *AJ*, **156**, 58
 Bath, G. T., Edwards, A. C., & Mantle, V. J. 1983, *MNRAS*, **205**, 171
 Bernat, A. P. 1981, *ApJ*, **246**, 184
 Bernat, A. P., Hall, D. N. B., Hinkle, K. H., et al. 1979, *ApJ*, **233**, 135
 Buckley, D. A. H., & Tuohy, I. R. 1989, *ApJ*, **344**, 376
 Bujarrabal, V., Alcolea, J., Mikołajewska, J., et al. 2018, *A&A*, **616**, L3
 Bujarrabal, V., Mikołajewski, J., Alcolea, J., et al. 2010, *A&A*, **516**, A19
 Burgarella, D., Vogel, M., & Paresce, F. 1992, *A&A*, **262**, 83
 Campbell, L. 1955, *Studies of Long Period Variables* (Cambridge: AAVSO)
 Catchpole, R. M., Robertson, B. S. C., Lloyd Evans, T. H. H., et al. 1979, *South Afr. Astron. Obs. Circ.*, **1**, 61
 Chapman, J. M., Sivagnanam, P., Cohen, R. J., & Le Squeren, A. M. 1994, *MNRAS*, **268**, 475
 Chen, Z., Frank, A., Blackman, E. G., Nordhaus, J., & Carroll-Nellenback, J. 2017, *MNRAS*, **468**, 4465
 Contini, M., & Formigini, L. 2003, *MNRAS*, **339**, 148
 Danchi, W. C., Bester, M., Degiacomi, C. G., et al. 1994, *AJ*, **107**, 1469
 de Val-Borro, M., Karovska, M., & Sasselov, D. D. 2009, *ApJ*, **700**, 1148
 de Val-Borro, M., Karovska, M., Sasselov, D. D., & Stone, J. M. 2017, *MNRAS*, **468**, 3408
 Eggleton, P. P. 1983, *ApJ*, **268**, 368
 Escorza, A., Siess, L., Van Winckel, H., et al. 2020, *A&A*, **639**, A24
 Gehrz, R. D., Evans, A., Helton, L. A., et al. 2015, *ApJ*, **812**, 132
 Gobrecht, D., Cherchneff, I., Sarangi, A., et al. 2016, *A&A*, **585**, A6
 Gregory, P. C., & Seaquist, E. R. 1974, *Natur*, **247**, 532
 Gromadzki, M., & Mikołajewska, J. 2009, *A&A*, **495**, 931
 Hajduk, M., Zijlstra, A., & Gesicki, K. 2008, *A&A*, **490**, L7
 Hall, D. N. B., Ridgway, S. T., Bell, E. A., & Yarborough, J. M. 1979, *Proc. SPIE*, **172**, 121
 Hartig, E., Lebzelter, T., Hinkle, K. H., & Mowlavi, N. 2022, *A&A*, in press
 Hinkle, K. H., & Barnes, T. G. 1979, *ApJ*, **227**, 923
 Hinkle, K. H., Brittain, S. D., & Lambert, D. L. 2007, *ApJ*, **664**, 501
 Hinkle, K. H., Fekel, F. C., Joyce, R. R., et al. 2013, *ApJ*, **770**, 28
 Hinkle, K. H., Hall, D. N. B., & Ridgway, S. T. 1982, *apj*, **252**, 697
 Hinkle, K. H., Lebzelter, T., & Straniero, O. 2016, *ApJ*, **825**, 38
 Hinkle, K. H., Wilson, T. D., Scharlach, W. W. G., et al. 1989, *AJ*, **98**, 1820
 Hoard, D. W., Ladjal, D., Stencel, R. E., & Howell, S. B. 2012, *ApJ*, **748**, L28
 Höfner, S. 2007, in *Why Galaxies Care About AGB Stars: Their Importance as Actors and Probes*, ed. F. Kerschbaum, C. Charbonnel, & R. F. Wing (ASP: San Francisco, CA), **145**
 Hoffleit, D., & Jaschek, C. 1982, *The Bright Star Catalogue* (4th edn.; New Haven, CT: Yale University Observatory)
 Hollis, J. M., Kafatos, M., Michalitsianos, A. G., et al. 1985, *ApJ*, **289**, 765
 Home, K., & Marsh, T.R. 1986, *MNRAS*, **218**, 761
 Ireland, M. J., Monnier, J. D., Tuthill, P. G., et al. 2007, *ApJ*, **662**, 651
 Ivison, R. J., Yates, J. A., & Hall, P. J. 1998, *MNRAS*, **295**, 813
 Jurkic, T., & Kotnik-Karuzza, D. 2018, *AstL*, **44**, 265
 Kafatos, M., & Michalitsianos, A. G. 1982, *Natur*, **298**, 540
 Karovska, M. 2006, in *Proceedings of The X-ray Universe 2005* (ESA SP-604), ed. A. Wilson, Vol. 604 (Noordwijk: ESA), **183**
 Keenan, P. C., Garrison, R. F., & Deutsch, A. J. 1974, *ApJS*, **28**, 271
 Kenyon, S. J., Fernandez-Castro, T., & Stencel, R. E. 1988, *AJ*, **95**, 1817
 Kloppenborg, B., Stencel, R., Monnier, J. D., et al. 2010, *Natur*, **464**, 870
 Kloppenborg, B. K., Stencel, R. E., Monnier, J. D., et al. 2015, *ApJS*, **220**, 14
 Knapp, G. R., Dobrovolsky, S. I., Ivezić, Z., et al. 1999, *A&A*, **351**, 97
 Knapp, G. R., & Morris, M. 1985, *ApJ*, **292**, 640
 Kurochkin, N. E. 1976, *SvAL*, **2**, 169
 Lee, Y. M., Kim, H., & Lee, H.-W. 2022, *ApJ*, **931**, 142
 Liimets, T., Corradi, R. L. M., Jones, D., et al. 2018, *A&A*, **612**, A118
 Liu, Z.-W., Stancliffe, R. J., Abate, C., et al. 2017, *ApJ*, **846**, 117
 Mattei, J. A., & Allen, J. 1979, *JRASC*, **73**, 173
 Mayer, A., Jorissen, A., Kerschbaum, F., et al. 2013, *A&A*, **549**, A69
 Meier, S. R., & Kafatos, M. 1995, *ApJ*, **451**, 359
 Melnikov, S., Stute, M., & Eislöffel, J. 2018, *A&A*, **612**, A77
 Menten, K. M., Lundgren, A., Belloche, A., et al. 2008, *A&A*, **477**, 185
 Merrill, P. W. 1935, *ApJ*, **81**, 312
 Merrill, P. W. 1950, *ApJ*, **112**, 514
 Michalitsianos, A. G., Oliverson, R. J., Hollis, J. M., et al. 1988, *AJ*, **95**, 1478
 Millan-Gabet, R., Pedretti, E., Monnier, J. D., et al. 2005, *ApJ*, **620**, 961
 Min, C., Matsumoto, N., Kim, M. K., et al. 2014, *PASJ*, **66**, 38
 Mohamed, S., & Podsiadlowski, P. 2007, in *ASP Conf. Ser.*, **372**, XV
 European Workshop on White Dwarfs, ed. R. Napiwotzki & M. R. Burleigh (San Francisco, CA: ASP), **397**
 Mohamed, S., & Podsiadlowski, P. 2012, *BaltA*, **21**, 88
 Muthumariappan, C., Parthasarathy, M., Leadbeater, R., et al. 2014, *MNRAS*, **445**, 2884
 Nagae, T., Oka, K., Matsuda, T., et al. 2004, *A&A*, **419**, 335
 Omelian, E., Sankrit, R., Helton, L. A., et al. 2020, *ApJ*, **898**, 31
 Parthasarathy, M., & Muneer, S. 2019, *Info. Bull. Var. Stars*, **6258**, 1
 Pearson, R. L., & Stencel, R. E. 2015, *ApJ*, **798**, 11
 Perets, H. B., & Kenyon, S. J. 2013, *ApJ*, **764**, 169
 Perrin, G., Cotton, W. D., Millan-Gabet, R., & Mennesson, B. 2015, *A&A*, **576**, A70
 Pilachowski, C. A., Hinkle, K. H., Young, M., et al. 2017, *PASP*, **129**, 24006
 Plavec, M., & Kratochvil, P. 1964, *BAICz*, **15**, 165
 Ragland, S., Le Coroller, H., Pluzhnik, E., et al. 2008, *ApJ*, **679**, 746
 Ramstedt, S., Mohamed, S., Olander, T., et al. 2018, *A&A*, **616**, A61
 Rattenbury, N. J., Wyrzykowski, Ł., Kostrzewa-Rutkowska, Z., et al. 2015, *MNRAS*, **447**, L31
 Rayner, J. T., Tokunaga, A., Jaffe, D., et al. 2022, *PASP*, **134**, 015002
 Reid, M. J., & Menten, K. M. 1997, *ApJ*, **476**, 327
 Saladino, M. I., Pols, O. R., & Abate, C. 2019, *A&A*, **626**, A68
 Saladino, M. I., Pols, O. R., van der Helm, E., et al. 2018, *A&A*, **618**, A50
 Schmid, H. M., Bazzon, A., Milli, J., et al. 2017, *A&A*, **602**, A53
 Smak, J. 1981, *AcA*, **31**, 395
 Solf, J., & Ulrich, H. 1985, *A&A*, **148**, 274
 Stencel, R. E., Blatherwick, R. D., & Geballe, T. R. 2015, *AJ*, **149**, 109
 Stencel, R. E., Kloppenborg, B. K., Wall, R. E., Jr., et al. 2011, *AJ*, **142**, 174
 Strassmeier, K. G., Weber, M., Granzer, T., et al. 2014, *AN*, **335**, 904
 Struve, O., Pillars, H., & Zeberg, V. 1958, *ApJ*, **128**, 287
 Teyssier, F., Boyd, D., Sims, F., et al. 2019, *ESIL*, **43**, 19
 Theuns, T., & Jorissen, A. 1993, *MNRAS*, **265**, 946
 Warner, B. 1995, *Cataclysmic Variable Stars* (Cambridge: Cambridge Univ. Press)
 Webster, B. L., & Allen, D. A. 1975, *MNRAS*, **171**, 171
 Whitelock, P. A. 1987, *PASP*, **99**, 573
 Whitelock, P. A., Feast, M. W., Catchpole, R. M., Carter, B. S., & Roberts, G. 1983, *MNRAS*, **203**, 351
 Whitelock, P. A., Feast, M. W., & Van Leeuwen, F. 2008, *MNRAS*, **386**, 313
 Whitelock, P., Marang, F., & Feast, M. 2000, *MNRAS*, **319**, 728

Willson, L. A., Gamavich, P., & Mattei, J. A. 1981, *Inf. Bull. Var. Stars*
No., 1961

Woodruff, H. C., Ireland, M. J., Tuthill, P. G., et al. 2009, *ApJ*, 691, 1328
Xu, S., Zhang, B., Reid, M. J., et al. 2019, *ApJ*, 875, 114